https://doi.org/10.5194/essd-2026-221
Preprint. Discussion started: 13 May 2026

Open Access Earth System Science Data Discussions

PROMICE: Greenland ice velocity maps v2026

Anne Solgaard[1], Anders Kusk[2], John Peter Merryman Boncori[2], Jørgen Dall[2], Andreas P. Ahlstrøm[1], Signe B. Andersen[1], Michele Citterio[1], Penelope How[1], Nanna B. Karlsson[1], Kristian K. Kjeldsen[1], Signe H. Larsen[1], Mads C. Lund[1], Anja Løkkegaard[1], Martin P. Lüthi[3], Jessica Mejia[4], Kenneth D. Mankoff[5,6], Dirk van As[1,7], Shin Sugiyama[8], and Robert S. Fausto[1]

[1]The Geological Survey of Denmark and Greenland, Østervoldgade 10, 1350 København K, Danmark
[2]Technical University of Denmark - National Space Institute, Ørsteds Plads 348, 2800 Kongens Lyngby, Denmark
[3]University of Zürich, Winterthurerstrasse 190, CH-8057 Zürich, Switzerland
[4]Department of Earth and Environmental Sciences, Syracuse University, Syracuse, NY, USA
[5]NASA Goddard Institute for Space Studies, New York, NY, 10025 USA
[6]Autonomic Integra LLC, New York, NY, 10025 USA
[7]Ice and Climate Research Organization (ICRO), Kangerlussuaq, Greenland
[8]Institute of Low Temperature Science / Arctic Research Center, Hokkaido University, Nishi 8, Kita 19, Sapporo, Japan

Correspondence: Anne Solgaard (aso@geus.dk)

Abstract. We present an updated version of the Programme for Monitoring of the Greenland Ice Sheet (PROMICE) ice velocity product (https://doi.org/10.22008/FK2/K70OPK; Solgaard and Kusk (2026)), providing a continuous time series of Greenland Ice Sheet velocity mosaics from January 2016 to the present. The product is derived from Sentinel-1 synthetic aperture radar (SAR) data, gridded at 200 m spatial resolution and updated every 12 days using data spanning two consecutive Sentinel-1 repeat cycles (24 days). Data are typically released within 10 days of the final acquisition and include all valid 6- and 12-day image pairs within the 24-day window.

This update includes several important improvements to the processing chain. The spatial resolution has been refined from 500 m to 200 m, justified by the implementation of an adaptive correlation template size approach for offset tracking, improving velocity retrievals and enhancing delineation of narrow outlet glaciers. We further implement a new mosaicking strategy, which reduces noise associated with ionospheric disturbances. Additional improvements include enhanced error handling and outlier rejection. The full processing workflow is described, including data selection, mosaicking, uncertainty estimation, and filtering procedures.

Validation against in-situ GNSS measurements over the full time series shows that the standard deviation of the differences between satellite- and GNSS-derived velocities (with corresponding bias) is 22 m/yr (-0.3 m/yr) and 38 m/yr (-0.4 m/yr) for the easting and northing components, respectively. These values fall within expected ranges, although a substantial fraction of the discrepancy likely reflects uncertainty in the GNSS measurements. This interpretation is supported by validation over stable terrain, where substantially lower values are obtained: 9 m/yr (0.1 m/yr) and 15 m/yr (-0.1 m/yr) for the easting and northing components, respectively. Compared to the previous product version, uncertainties are higher due to a prolonged period when only one Sentinel-1 satellite was operational, resulting in increased noise and reduced temporal sampling. We quantify the impact of these conditions on spatial coverage.

https://doi.org/10.5194/essd-2026-221
Preprint. Discussion started: 13 May 2026

Open Access Earth System Science Data Discussions

Overall, coverage is highest during winter, when radar coherence is strong and acquisitions are most comprehensive, whereas summer coverage is reduced due to surface melt. Despite these seasonal and mission-related constraints, the PROMICE ice velocity product provides consistent temporal sampling and broad spatial coverage, supporting investigations of ice-sheet-wide and glacier-specific dynamics and ice discharge on seasonal to multi-year timescales.

1 What is new in this edition

The Programme for Monitoring of the Greenland Ice Sheet (PROMICE) ice velocity product is a living data product that updates regularly, approximately every 12 days, and undergoes continuous development. Since the last reference paper (Solgaard et al., 2021) several important improvements to the processing chain have been carried out. For clarity in the rest of the manuscript, we will refer to the former data product version as v2021 and this updated version as v2026. In the following, we detail all updates to the dataset but here we highlight two important updates in particular:

1. The spatial posting has been reduced from 500 m to 200 m.
2. Noise from ionospheric effects has been reduced.

The refinement in spatial posting is justified by implementing an adaptive correlation template size when performing the cross correlation to estimate shifts between two Sentinel-1 SLC images. This increases the spatial resolution where smaller correlation templates can be applied and has especially improved the delineation of the velocity field at narrow marine-terminating outlet glaciers, thereby resolving issues of spurious slowdowns and poorly resolved dynamics close to the margins of some of these glaciers.

The method presented in Andersen et al. (2020) for producing mosaics from multiple offset-tracking results (See Sect. 5.3) has been implemented. Importantly, this leads to a reduction in noise stemming from ionospheric effects in areas with input from crossing tracks, and it facilitates production of mosaics with input from different data sources.

We validate the updated product (v2026) against in situ GNSS (Global Navigation Satellite System) measurements to assess its quality and examine how the period with only a single operational Sentinel-1 satellite affected product performance. In Solgaard et al. (2021), the PROMICE ice velocity product was validated against GNSS measurements from PROMICE automatic weather stations (AWS) located mainly in the ablation zone of the GrIS (Fausto et al., 2025). This data is sparse due to the difficulty in collecting this type of measurement, and furthermore the observations are commonly acquired for other purposes than validation of glacier flow. However, for this updated dataset an effort was made to include more sources of validation data to cover more regions of the ice sheet both in a geographical sense, but most importantly to cover a larger range of velocity magnitudes, as the PROMICE AWS network is intentionally located in slow-flowing areas.

This paper focuses on the implementation and impacts of the points listed above, and we refer product users to Solgaard et al. (2021) for more details about the product.

https://doi.org/10.5194/essd-2026-221
Preprint. Discussion started: 13 May 2026

Open Access Earth System Science Data Discussions

2 Introduction

Satellite observations have revolutionized our ability to monitor ice-sheet-wide velocity, particularly since the launch of missions such as ESA's Sentinel-1 (2014, 2016, 2024, and 2025), Sentinel-2 (2015, 2017, and 2024), and the joint NASA/USGS mission Landsat 8 (2013) and 9 (2021). The availability of the vast amounts of freely accessible data has greatly increased the temporal and spatial coverage of ice velocity products. These platforms have now provided more than a decade of consistent observations, enabling the generation of long time series of ice velocity maps with varying spatial and temporal characteristics (Joughin, 2020b; Solgaard et al., 2021; Wuite et al., 2026). Prior to this, surface ice velocity maps of the Greenland Ice Sheet (GrIS) and its outlet glaciers only resolved annual or seasonal characteristics due to the limited availability of data (e.g. Howat et al., 2010; Joughin et al., 2010; Moon et al., 2014; Rignot and Kanagaratnam, 2006).

The flow of ice sheets and glaciers vary on a range of different time scales in response to the seasonal cycle, climate change and internal variability (e.g. Moon et al., 2020; Joughin et al., 2018; Mouginot et al., 2018). For this reason, different types of ice velocity products are relevant depending on the purpose of the study. For example, short-timescale products derived from individual image pairs (e.g. NASA MEaSUREs ITS_LIVE (Gardner et al., 2019, 2025)) can capture rapid changes in ice motion but often suffer from limited spatial coverage at a given point in time. In contrast, ice-sheet-wide mosaics with sparse gaps provide a more complete spatial coverage but are typically produced from data acquired over longer time periods, ranging from weeks to years, resulting in reduced temporal resolution, e.g. annual, quarterly, monthly and bi-weekly mosaics from Copernicus Climate Change Service and ESA Climate Change Initiative (Nagler et al., 2015; Wuite et al., 2026) and NASA's MEaSUREs program (e.g. Joughin, 2020a, c, b).

In-situ measurements of ice-flow velocities (e.g. from GNSS) are relatively sparse on the GrIS and are often of short duration (subannual) at high temporal resolution (e.g. Khan et al., 2022; Sole et al., 2011; Maier et al., 2019; Sugiyama et al., 2025) or of longer duration (years) but at low temporal resolution (e.g. Hvidberg et al., 2020; Thomas et al., 1998). A few span several years at high temporal resolution (e.g. Ahlstrøm et al., 2013; Fausto et al., 2025). The sparseness is due to the inaccessibility and size of the GrIS and harsh climatic conditions, which make fieldwork and instrumentation challenging. While satellite observations are essential for providing continuous observations over large areas, in-situ observations are key for studying processes at the sub-daily scale as well as for providing ground truth for satellite-derived products.

In this paper we describe updates outlined in Sect. 1 to the PROMICE Ice Velocity product since the first reference paper (Solgaard et al., 2021). The PROMICE Ice Velocity product is developed as part of the PROMICE programme with the primary objective to monitor GrIS dynamics and track solid ice discharge from the marine terminating glaciers (Mankoff et al., 2020) — a key part of the total ice sheet mass balance. The product is a compromise between obtaining coverage of the entire GrIS margin at as high temporal resolution as possible, while still upholding sufficient coverage.

Beyond its core purpose, the PROMICE Ice Velocity product has been applied in a wide range of scientific applications. These include investigations of seasonal variability in ice flow (Solgaard et al., 2022; Vijay et al., 2019), studies of glacier response in a changing climate (Brough et al., 2023; Khan et al., 2022), comparisons with independent velocity datasets (Davison et al., 2020), and use as a reference in interferometric synthetic aperture radar analyses (Andersen et al., 2025). It has

https://doi.org/10.5194/essd-2026-221
Preprint. Discussion started: 13 May 2026

also been combined with ice-flow modelling to examine processes such as ice shelf stability, subglacial hydrology, and to infer ice thickness of a smaller ice cap (Khan et al., 2024; Koldtoft et al., 2021; Rathmann et al., 2017).

3 The PROMICE ice velocity Product

The PROMICE ice velocity product (https://doi.org/10.22008/FK2/K70OPK (Solgaard and Kusk, 2026)) is a geospatial time series of Greenland-wide ice velocity mosaics produced using the Interferometric Post Processing (IPP) processor (see Sect.5). The product spans the period from January 2016 to the present, has a grid spacing of 200 m, and a temporal resolution of 24 days. The effective spatial resolution is on the order of 400-900 m, determined by the adaptive size of the correlation windows used in the offset-tracking (see Sect. 5.1). Thus, glaciers smaller than approximately 1 km across will not be fully resolved. The product is based on measurements of displacements between pairs of radar images acquired 6 or 12 days apart (see Sect. 4.1). To achieve a consistent coverage (see Sect. 7), each mosaic is based on velocity measurements from all possible 6- and 12-day pairs using data from Sentinel-1A, 1B and 1C within two consecutive Sentinel-1A orbit cycles (i.e. 24 days). In the period between December 2021, when Sentinel-1B malfunctioned, and March 2025, when Sentinel-1C data became available, the PROMICE product is only based on 12-day pairs from Sentinel-1A. This has implications for the product, resulting in reduced spatial coverage and increased noise during the period. This is discussed further in Sect. 7 and 8. A new map is produced for every Sentinel-1A cycle, i.e. a new mosaic every 12 days, and a given mosaic thus overlaps with the previous and subsequent maps by 12 days.

The dataset is expanded continuously, and we aim to provide a new mosaic within 10 days of the last acquisition. However, this lag may be larger during the winter campaigns when more data is acquired. The velocity provided at every grid point in the PROMICE ice velocity product is the weighted average of all velocity measurements available at that grid point within that 24-day period (see Sect. 5.3), and should therefore be considered as a 24-day average estimate of velocity. The start and end times of this period are given in the *time_bnds* variable in the NetCDF product (see Table 1). Figure 1 shows samples from the timeseries of the first mosaic of every year since 2016.

Each ice velocity mosaic is supplied as a single NetCDF file following the Climate Forecast (CF) conventions (see https://cfconventions.org/). The mosaics are provided on a 200 m Polar Stereographic Greenland-wide grid with latitude of true scale at 70°N and reference longitude -45°E (EPSG 3413 projection). The variables in the NetCDF product are listed in Table 1. A quick look image for each mosaic is provided along with the dataset.

4 Data

In the following, we present the characteristics of the Sentinel-1 data and introduce the input data that we use to generate the PROMICE ice velocity product.

https://doi.org/10.5194/essd-2026-221
Preprint. Discussion started: 13 May 2026

Open Access Earth System Science Data Discussions

Table 1. Variables in the PROMICE ice velocity NetCDF product

Variable	Description	Unit
x	x-coordinate of projection	m
y	y-coordinate of projection	m
time	Midpoint time of all contributing acquisitions	Days since 1990-1-1
time_bnds	First and last time of contributing acquisitions	Days since 1990-1-1
land_ice_surface_easting_velocity	Ice velocity along x-axis	m/d
land_ice_surface_northing_velocity	Ice velocity along y-axis	m/d
land_ice_surface_vertical_velocity	Vertical velocity from surface parallel flow	m/d
land_ice_surface_velocity_magnitude	Horizontal ice velocity magnitude	m/d
land_ice_surface_easting_velocity_std	Ice velocity error estimate along x-axis	m/d
land_ice_surface_northing_velocity_std	Ice velocity error estimate along y-axis	m/d
land_ice_surface_velocity_magnitude_std	Horizontal ice velocity error estimate	m/d

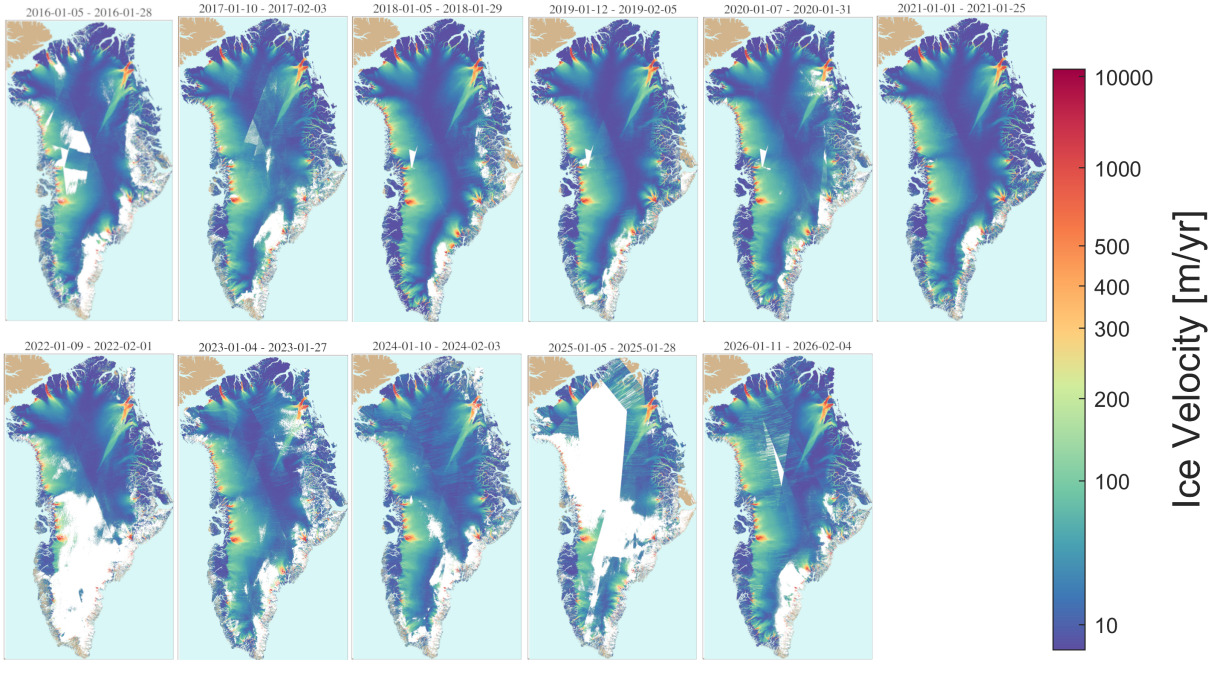

Figure 1. Examples of the PROMICE v2026 ice velocity maps (in metres per year), showing the first map of each year from 2016 to 2026. The 2022 and 2025 mosaics shown were derived only from Sentinel-1A scenes, demonstrating the product's sensitivity to the number of operational satellite image sources.

https://doi.org/10.5194/essd-2026-221
Preprint. Discussion started: 13 May 2026

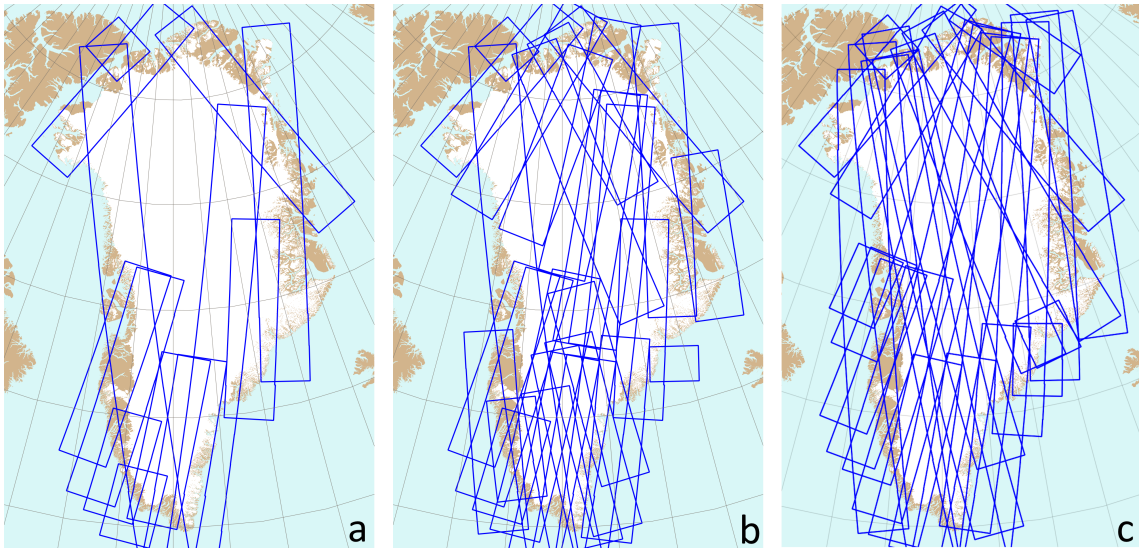

Figure 2. Typical Sentinel-1 coverage over Greenland for a single 12-day orbital cycle, a) during the standard observation scenario for Sentinel-1A and Sentinel-1B (2016-2021), b) during the dedicated winter campaign from December 2019 - February 2020, c) After commissioning of Sentinel-1C in May 2025. The blue polygons represent acquisitions from different tracks, acquired at different times during the cycle.

4.1 Sentinel-1 SAR Data Characteristics

SAR sensors are well-suited for polar observations because data collection is not impacted by the polar night or cloud cover. At the time of writing (April 2026), the Sentinel-1 constellation consists of three operational satellites (this has varied as described in the previous section), Sentinel-1A, Sentinel-1C, and Sentinel-1D equipped with identical C-band (5.4 GHz) SAR sensors, and in near-polar orbits with a repeat cycle of 175 orbits, corresponding to 12 days. The orbits are phased so that Sentinel-1C repeats the ground track of Sentinel-1A after 6 days, and Sentinel-1D repeats the ground track of Sentinel-1C after 1 day. In July 2026, it is expected that Sentinel-1A will be phased out, returning to a nominal two-satellite constellation with 6 days between Sentinel-1C and Sentinel-1D. From 2016-2025, the margins were covered every 12 days (Fig. 2a), and the entire ice sheet was mapped from several additional tracks every winter from December to February, allowing the generation of Greenland-wide maps during this season (Fig. 2b). With the current observation schedule as of May 2025, the entire ice sheet is imaged every 12 days (Fig. 2c), with temporary additional coverage from Sentinel-1D.

Image pairs can be formed between acquisitions from the same satellite, e.g., S1A-S1A and S1C-S1C, with temporal baselines that are multiples of 12 days (12 days, 24 days, etc.). In addition, image pairs can be formed from acquisitions obtained from two different satellites, e.g., S1A-S1B, with a temporal baseline that is an odd multiple of 6 days (6 days, 18 days, etc.). For a limited period (expected April-June 2026), 1-day baselines can be achieved between Sentinel-1C and Sentinel-1D.

https://doi.org/10.5194/essd-2026-221
Preprint. Discussion started: 13 May 2026

4.2 Input Data

The data used to generate the PROMICE ice velocity product are single-look complex (SLC) IW radar images (with annotations), supplied by the Copernicus Data Space Ecosystem (https://dataspace.copernicus.eu/). They are supplied as slices with a footprint of approximately 250 km × 250 km and a resolution (3 m × 22 m) (range/azimuth). The SLC images are supplemented by restituted orbit files (also available on Copernicus Data Space), available a few hours after acquisition, and instrument timing calibration files from (Center, 2026). The Tandem-X global 90 m DEM (DLR, 2018) is employed for geocoding and coregistration, and the coregistration is additionally supported by a multi-year average of existing PROMICE ice velocity maps (see Sect. 5.1).

5 Methods

The data processing is carried out using the Interferometric Post-Processing Chain (IPP) processor, developed and maintained by DTU Space (Kusk et al., 2018). Despite the name, the processor also performs offset-tracking for displacement measurements, which is the functionality used to generate the PROMICE ice velocity data product. Relative to the v2021 of the PROMICE IV product (Solgaard et al., 2021), a number of improvements have been made to increase spatial resolution and reduce the impact of ionospheric effects on the product, described in the following sections. A high-level overview of the processing flow is shown in Fig. 3a.

As described in detail in Solgaard et al. (2021), Sect. 4, product generation relies on a local database of all available IW SLC products, updated regularly by searching the Copernicus Data Space Catalog and downloading new products. A single output velocity map is a mosaic based on offset-tracking of SLC pairs from all Sentinel-1 observations carried out within two consecutive Sentinel-1A orbit cycles (24 days), containing both 6- and 12-day pairs (and, for a limited period with Sentinel-1A, -B, and -C available, 1- and 13-day pairs). When Sentinel-1A is phased out, the reference period delineating input data for a product will be changed to be based on two Sentinel-1C or Sentinel-1D orbital cycles.

When all pairs required for a product have been processed using the approach in Sect. 5.1, the geocoding and error estimation described in Sect. 5.2 and 6 is performed for each pair, followed by fusion and mosaicking of all the pairs, as described in Sect. 5.3.

5.1 Offset-tracking

The offset-tracking procedure estimates local shifts between two SLC images in radar geometry using normalized cross-correlation (NCC) of intensity image patches (Fig. 3b).

The SLC with the earliest acquisition time is used as the reference image (SLC1). Prior to offset-tracking, calibration constants in range and azimuth timing are applied to correct for the different geolocation biases observed in the products for the different Sentinel-1 satellites (see Sect. 5.2), and the second image (SLC2) is coregistered (resampled) to the geometry of the reference image, using orbit information, the DEM, and an external ice velocity map (a multi-year average of existing

https://doi.org/10.5194/essd-2026-221
Preprint. Discussion started: 13 May 2026

Open Access Earth System Science Data Discussions

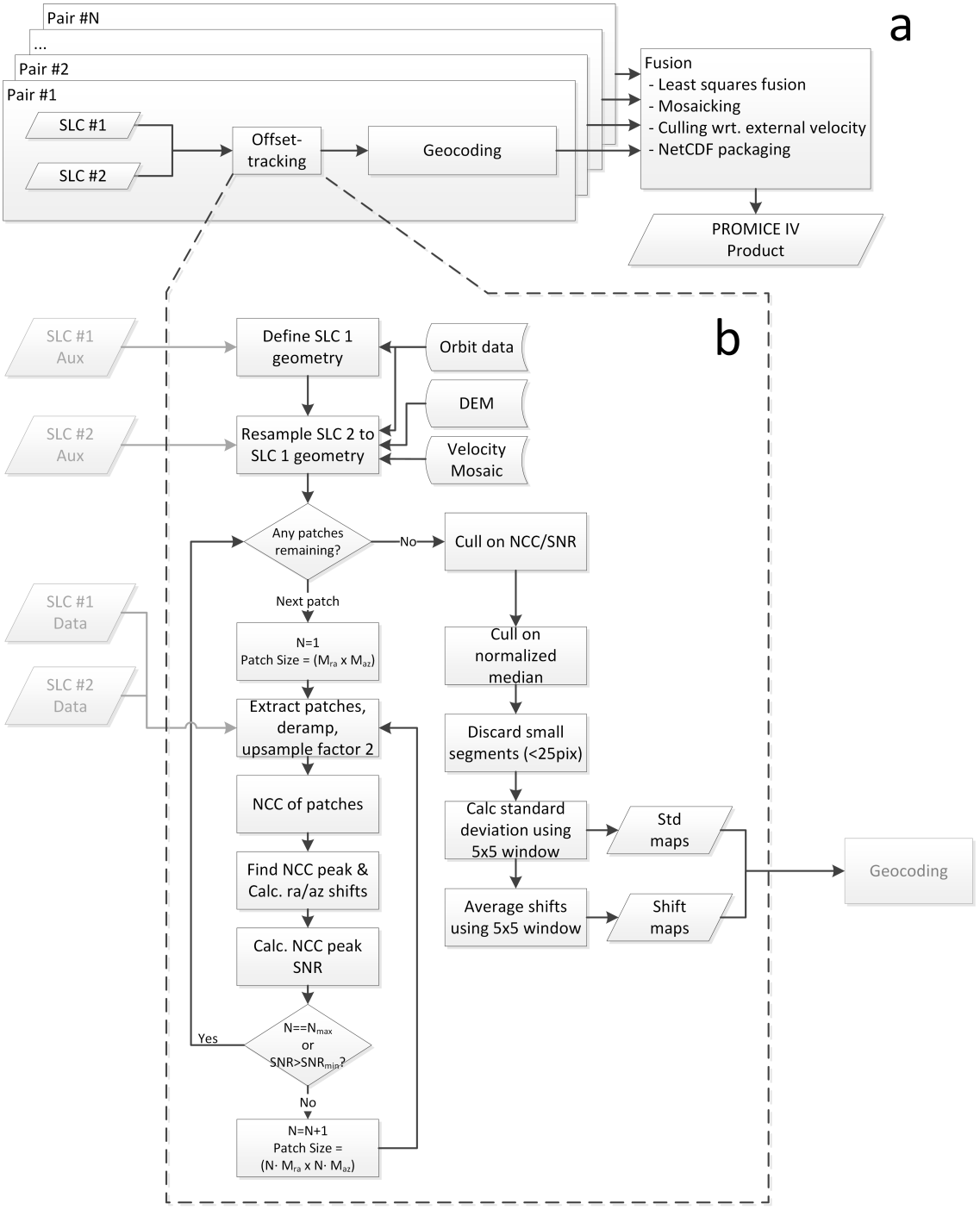

Figure 3. Processing flow for PROMICE ice velocity product, a) High level processing flow, b) Offset-tracking details.

https://doi.org/10.5194/essd-2026-221
Preprint. Discussion started: 13 May 2026

PROMICE velocity products). In v2021 of the product, the input SLCs were not coregistered prior to offset-tracking, but coregisteration improves coherence for homogeneous scenes where offset estimation relies on speckle (see Solgaard et al. (2021) Sect. 5.3). Using an external velocity map improves the correlation estimate in patches containing both moving and stationary pixels (e.g., at boundaries between glacier and rock), since each pixel is individually resampled. The initial shift estimate from the external velocity map used to coregister the SLCs is added to the shift estimated from the NCC procedure (described below) to achieve the final estimate.

An output grid is defined in the reference image geometry, with a spacing of 40 pixels in the slant-range direction and 10 pixels in the along-track (azimuth) direction. These spacings correspond to approximately 150 m×150 m on the ground, and are unchanged from v2021 of the product.

Offset-tracking is carried out for each grid point by cross-correlating image patches surrounding the grid points. An adaptive patch size is employed, meaning that for a given output grid point, the NCC is first carried out using a small template patch size (to achieve a good spatial resolution), but if this fails, the template patch size is increased and the calculation is repeated.

The NCC is done by extracting from SLC2, a patch (the NCC template) of size $M_{ra} \times M_{az}$ (slant range×azimuth). From the reference image, a patch (the NCC search window) of size $(M_{ra}+S_{ra}) \times (M_{az}+S_{az})$ pixels is extracted, where $S_{ra}+1$ is the number of range lags for which to calculate the NCC, and $S_{az}+1$ is the number of azimuth lags. The initial template size is set to $M_{ra} = 128$ and $M_{az} = 32$, giving an effective spatial resolution of 400-500 m. If a valid shift estimate is not obtained with this template size, the template size is increased to 256×64 (corresponding to the fixed template size used in v2021 of the PROMICE ice velocity data product).

Each patch is deramped (Miranda, 2017), upsampled by a factor of two (in both range and azimuth) using FFT interpolation, and the intensity (magnitude squared of the complex pixel values) is derived. A normalized cross-correlation of the two upsampled real-valued patches is carried out using the algorithm in (Lewis, 1995), resulting in a correlogram of size $(2 \cdot S_{ra}+1) \times (2 \cdot S_{az}+1)$ with values between 0 and 1. The integer shift between the two patches is then estimated by locating the peak of the correlation surface, and a 9×9 pixel neighbourhood surrounding the peak is upsampled by a factor of 4, again using FFT interpolation. Then the fractional shift is retrieved by fitting a parabola to the peak and its two surrounding pixels in each dimension, correcting finally for oversampling factors and accounting for the initially applied shift of SLC2 from the external velocity map. A signal-to-noise ratio (SNR) for the peak estimate is calculated by dividing the correlation value of the peak with the mean of the surrounding pixels in the correlation surface (de Lange et al., 2007). If the SNR is below 5, the result is rejected, and the above procedure is repeated once with an increased template and search window sizes achieved by multiplying M_{ra} and M_{az} by a factor of two. After either one or two iterations, the estimated 2-D shift, the peak normalized cross correlation value (NCC), and the SNR are all saved for further processing.

The procedure described above will yield a shift estimate even if the two images are completely uncorrelated, so a culling of the estimated shifts is carried out. First, pixels with an SNR<5 are set as invalid. Then, a further culling, is carried out on the range and azimuth shifts, using a normalized median test, as described in (Westerweel and Scarano, 2005). For each measurement, U_0, in a 5×5 neighbourhood, the median, U_m, of the 24 surrounding measurements $(U_1, U_2, \ldots, U_{25})$ is calculated (excluding U_0), and for each measurement in the neighbourhood, a residual, $R_i = |U_i - U_m|$ is calculated. The median, R_m,

https://doi.org/10.5194/essd-2026-221
Preprint. Discussion started: 13 May 2026

of $(R_1, R_2, \ldots, R_{24})$ is then calculated, and used to normalize the residual of U_0 so that $R'_0 = |U_0 - U_m|/(R_m + \epsilon)$, where ϵ is a minimum normalization level that accounts for cross-correlation noise. We use $\epsilon = 0.1$ pixel, as suggested in (Westerweel and Scarano, 2005), and cull the measurement, U_0, if R'_0 exceeds a threshold of 5 for either of the range or azimuth shifts. This value was found by experiments to remove most clearly visible outliers, without removing valid measurements. Lower values removed more outliers, but had an adverse effect on measurement coverage. After the culling, small unconnected segments of pixels (<25 pixels) are removed, as these were found to often contain erroneous values. Some outliers may remain, especially in areas subject to surface melt, as the associated strong radar backscatter can create false correlation peaks. An additional culling based on time series statistics (see Sect. 5.3) is carried out on the final mosaicked product to further suppress these outliers.

For use in error estimation, the local standard deviations of the two shift maps (range and azimuth shifts) are estimated in a sliding 5×5 window, ignoring pixels with invalid measurements, and the shift maps are finally averaged by a 5×5 window. The shift maps (in units of SLC pixels) and associated standard deviations are stored along with the SLC parameters and orbit information to be used in the subsequent processing.

5.2 Geocoding

The geocoding takes as input the shift maps and associated standard deviation maps output by the offset-tracking and the DEM. Using the DEM and orbit information, the maps are interpolated to the output grid in map projection (see Sect. 3). The shifts and standard deviations are converted to velocity by multiplying with the SLC pixel spacing and dividing by the temporal baseline. At this stage, the velocities and standard deviations, even though provided on a georeferenced grid, are still measured in the radar range/azimuth geometry.

5.3 Fusion

The fusion step describes the process of combining and mosaicking the geocoded offset-tracking results on to a Greenland-wide grid. In v2021 of the PROMICE ice velocity product, the 2D surface velocities were first derived for each pair using range and azimuth offsets and the assumption of surface parallel flow (SPF), then subsequently combined with weighted averaging. In v2026 of the product, surface parallel flow is still assumed, but the fusion algorithm has been updated to the one described in Andersen et al. (2020), where all available observations for one output pixel are combined using a weighted least squares approach. In regions where observations from crossing orbits are available, the least squares fusion approach reduces the reliance on azimuth offsets, which have a lower resolution than the range offsets (see Sect. 4.1) and are often affected by ionospheric scintillations (see Sect. 6.1). For a pixel where only a offset-tracking single pair is available, the velocity and error estimates obtained with the v2021, and v2026 fusion approaches will be identical.

Let $\mathbf{v} = [v_x, v_y]^T$ be the 2D surface velocity vector in map geometry to be estimated. With the SPF assumption, the vertical velocity, v_z, can be written as Joughin et al. (1998):

$$v_z = \left(\frac{\partial z}{\partial x} v_x + \frac{\partial z}{\partial y} v_y\right) \tag{1}$$

https://doi.org/10.5194/essd-2026-221
Preprint. Discussion started: 13 May 2026

Open Access Earth System Science Data Discussions

where $(\frac{\partial z}{\partial x}, \frac{\partial z}{\partial y})$ is the surface gradient derived from the DEM.

We can now set up a weighted linear least squares problem, $\mathbf{u} = \mathbf{H}\mathbf{v} + \boldsymbol{\epsilon}$, which can be stated as Andersen et al. (2020):

$$\begin{bmatrix} v_{r1} \\ v_{a1} \\ \vdots \\ v_{rN} \\ v_{aN} \end{bmatrix} = \begin{bmatrix} \cos\theta_1 \cos\phi_1 + \sin\theta_1 \frac{\partial z}{\partial x} & \cos\theta_1 \sin\phi_1 + \sin\theta_1 \frac{\partial z}{\partial y} \\ -\sin\phi_1 & \cos\phi_1 \\ \vdots & \vdots \\ \cos\theta_N \cos\phi_N + \sin\theta_N \frac{\partial z}{\partial x} & \cos\theta_N \sin\phi_N + \sin\theta_N \frac{\partial z}{\partial y} \\ -\sin\phi_N & \cos\phi_N \end{bmatrix} \begin{bmatrix} v_x \\ v_y \end{bmatrix} + \boldsymbol{\epsilon} \tag{2}$$

where v_{rn} is the measured range velocity from pair number n, v_{an} is the corresponding azimuth velocity, and angles ϕ and θ describe the orientation of the range line-of-sight (LoS) vector pointing from the pixel under consideration to the sensor, with the horizontal angle ϕ measured counter-clockwise from the y-axis of the map projection and the elevation angle θ measured from the local horizontal plane to the LoS vector. Projection scaling factors are not applied to the velocities, so these represent physical velocities along the projection axes. The noise vector, $\boldsymbol{\epsilon}$, is assumed normally distributed with zero mean and diagonal covariance matrix Σ:

$$\Sigma_{v_{ra}} = \begin{bmatrix} \sigma_{r1}^2 & 0 & \cdots & 0 \\ 0 & \sigma_{a1}^2 & \cdots & 0 \\ \vdots & \vdots & \ddots & \vdots \\ 0 & 0 & \cdots & \sigma_{aN}^2 \end{bmatrix} \tag{3}$$

with σ_{rn} and σ_{an} indicating the estimated standard deviations of the range and azimuth measurements for pair n. The weighted least squares solution to this system is:

$$\hat{\mathbf{v}} = (\mathbf{H}^T \boldsymbol{\Sigma}_{\mathbf{v_{ra}}}^{-\mathbf{1}} \mathbf{H}) \mathbf{H}^T \boldsymbol{\Sigma}_{\mathbf{v_{ra}}}^{-\mathbf{1}} \mathbf{u} \tag{4}$$

and the resulting covariance matrix of the estimate is:

$$\Sigma_{v_{xy}} = \begin{bmatrix} \sigma_{v_x}^2 & \sigma_{v_{xy}} \\ \sigma_{v_{xy}} & \sigma_{v_y}^2 \end{bmatrix} = \mathbf{H}^T \boldsymbol{\Sigma}^{-1} \mathbf{H} \tag{5}$$

from which the error estimates for $\hat{\mathbf{v}}$, σ_{v_x} and σ_{v_y} can be retrieved as the square root of the diagonal elements.

The error estimate of the velocity magnitude, $\sigma_{v_{mag}}$ is also included in the product, obtained by:

$$\sigma_{v_{mag}} = \sqrt{\frac{v_x^2 \sigma_{v_x}^2 + v_y^2 \sigma_{v_y}^2 + 2 v_x^2 v_y^2 \sigma_{v_{xy}}}{v_x^2 + v_y^2}} \tag{6}$$

The effective resolution of the velocity maps is on the order of the NCC template patch size, which corresponds to approximately 400-900 m on ground (due to the adaptively varying patch size, see Sect. 5.1), so the resolution of the surface gradient map should approximately match this. The DEM is downsampled to the pixel spacing of the PROMICE ice velocity product (200 × 200 m), and the gradient is derived using second order differences, which means the gradients are derived using samples approximately 400 m apart.

https://doi.org/10.5194/essd-2026-221
Preprint. Discussion started: 13 May 2026

Open Access Earth System Science Data Discussions

5.4 Culling

Prior to fusing and mosaicking, culling is carried out on the individual pairs to remove further outliers. This is different from v2021, where culling was carried out after mosaicking, but the principle is the same. The culling relies on comparison of the measured value with an average value of all available measurements, based at the time of writing on nearly 10 years of data. For each pixel, we reject the measurement if:

$$\frac{\sqrt{(\hat{v}_x - v_{m,x})^2 + (\hat{v}_y - v_{m,y})^2}}{\sqrt{v_{m,x}^2 + v_{m,y}^2} + v_\epsilon} > k_{thr} \tag{7}$$

where $(\hat{v}_x, \hat{v}_y)$ is the velocity measurement of the individual pair, $(v_{m,x}, v_{m,y})$ is the average velocity, v_ϵ is a velocity constant preventing erroneous culling in areas with very low velocities, and k_{thr} is a constant factor, setting the threshold for culling. A low value of k_{thr} will remove more outliers, but may also remove valid measurements in areas with strong seasonal amplitudes and glaciers with significant intra-annual or inter-seasonal variability. This was explored in Solgaard et al. (2021). We apply $v_\epsilon = 20$ m/yr and a value of k_{thr}=5. For comparison, the mosaics in the v2021 data were produced using a value of k_{thr}=3 and the same value for v_ϵ (Solgaard et al., 2021). The impact of culling is discussed in Sect. 7.

6 Error Sources and Error Estimation

The PROMICE ice velocity product is subject to several sources of error. The treatment and characterization of most of these sources remain unchanged since v2021, and we refer to Solgaard et al. (2021) for a detailed description. These errors can be grouped into five main categories:

1. Slowly varying errors, such as those caused by orbit errors or other timing biases in the products (refer to Solgaard et al. (2021) Sect. 5.1 and 5.2). At the time of writing, timing calibration constants from Center (2026) are used, but those provided for Sentinel-1C and 1D are for now set to zero and might be updated in the future.
2. Temporal decorrelation caused by changes in the radar backscatter between observations (refer to Solgaard et al. (2021) Sect. 5.3).
3. Ionospheric errors, resulting in localized, but spatially correlated errors in the measured azimuth shift (see Sect. 6.1).
4. Aliasing errors caused by the need to acquire two observations from which we infer displacement, and then velocity. Any extreme velocity highs or lows will be smoothed out.
5. Errors due to tidal motion of floating glacier tongues (refer to Solgaard et al. (2021) Sect. 5.5).

The error estimates provided with the PROMICE ice velocity product are derived from the local standard deviation of the underlying shift maps generated by the offset-tracking (see Sect. 5.1 and 5.3). As such, they do not account the for slowly varying errors, such as orbit errors and timing biases, and only to a limited extent for the impact of ionospheric errors, as these

https://doi.org/10.5194/essd-2026-221
Preprint. Discussion started: 13 May 2026

are locally correlated on the scale of the window size used to estimate the local standard deviations. Although this is not a complete error characterization, it was shown in Boncori et al. (2018) to provide the correct order of magnitude for the errors.

The slowly varying errors could potentially be corrected by calibrating the measured velocities using ground control points (GCPs), either on stable terrain or in areas where ice flow is known to vary little. In practice, this is difficult to achieve in an automated system, as calibration must be performed on individual pairs, where the ionospheric and, to some extent, the temporal decorrelation errors associated with offset-tracking are often much larger than the slowly varying errors. If GCPs are unwittingly selected in areas affected by e.g. ionosphere, the GCP calibration could actually have a detrimental impact. A large number of GCPs, well distributed across the image, would be required to reduce statistical noise, but this is often not feasible within the limited spatial coverage of a single pair. For this reason, the PROMICE ice velocity product is not calibrated using GCPs.

Compared to v2021, ionospheric impact is reduced in specific settings in v2026. This is discussed below.

6.1 Ionospheric Errors

Ionospheric propagation errors arise due to spatial fluctuations (scintillations) in the ionosphere's total electron content (TEC) within the SAR synthetic aperture length (i.e. km-scale variations) (Gray et al., 2000). As detailed in Solgaard et al. (2021), Sect. 5.4, these can cause slowly varying azimuth shifts between two acquisitions, translating to errors in velocity estimates that can exceed 300 m/yr in extreme cases. With the fusion approach introduced in the v2026 product (described in Sect 5.3), we exploit the fact that in some regions, measurements from both ascending and descending tracks are available, and in this case, ice velocities can be derived primarily from the range offsets, which are much less sensitive to ionospheric effects than azimuth offsets and also considerably less noisy, owing to the fact that the range resolution of Sentinel-1 is 7 times higher than the azimuth resolution. A comparison of the original and the new approach applied to the same input data (Fig. 4), shows that the new approach reduces the ionosphere streaks significantly in the central area where the ascending and descending tracks overlap. In the standard S1 IW acquisition scenario up to May 2025 (Fig. 2a), only two ascending tracks were acquired (the long track along the west coast of Greenland, and the track covering the northeast margin of the ice sheet up to the northernmost point), so the method is not always applicable everywhere, but during the winter campaigns (Fig. 2b), and with the standard observation scenario as of May 2025 (Fig. 2c), this method is applicable over large parts of the ice sheet.

Where observations from crossing tracks are not available, the mitigation of ionospheric effects in the PROMICE ice velocity product relies on culling and averaging. Pixels with large ionospheric errors, if present in regions with generally low velocities, will be removed by the temporal culling procedure described in Sect. 5.3. In areas where multiple velocity observations are available, the weighted averaging in the fusion (see Sect. 5.3) will tend to reduce, but not completely remove, the ionospheric effects. We estimate that ionospheric effects can cause a velocity error of up to 300 m/yr and will mainly affect the v_y-component, which is roughly aligned with the azimuth direction due to the near-polar orbit of the Sentinel-1 satellites.

https://doi.org/10.5194/essd-2026-221
Preprint. Discussion started: 13 May 2026

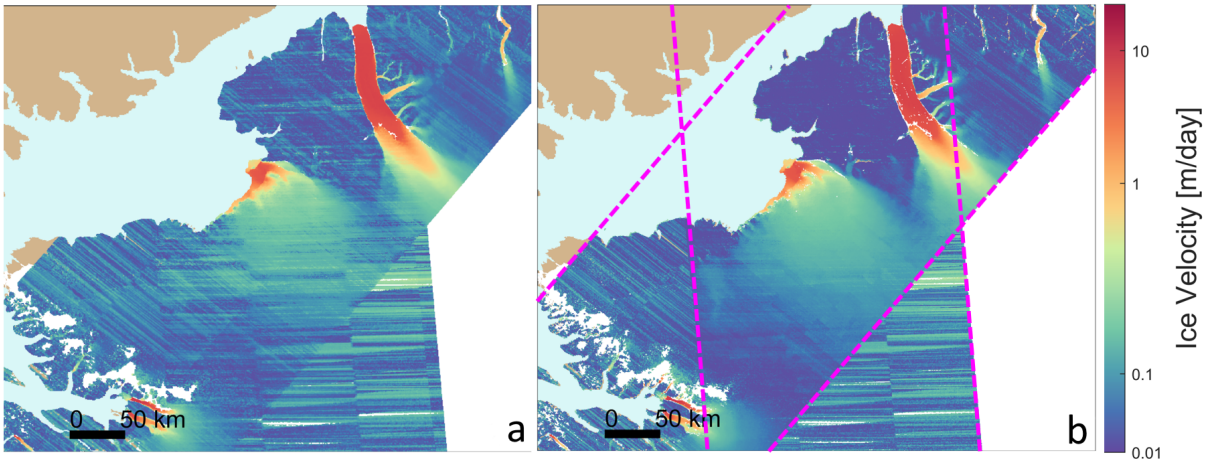

Figure 4. Example from Northwest Greenland showcasing the reduction of ionospheric impact with crossing tracks: (a) v2021 of the product posted at 500 m resolution. (b) Same input data processed using the new version of the processor (v2026) posted at 200 m resolution, with purple dashed lines indicating track boundaries. Ionospheric streaks are visibly reduced in the intersection of the tracks.

7 Product Characteristics and Impact of the Updates to the Processing Chain

7.1 Enhanced delineation

In version v2021 of the product, several outlet glaciers—particularly in southeast Greenland—exhibited episodes of spurious slowdowns and a reduced ability to capture flow near the outlet margins when compared with optical imagery. An example is shown in Fig. 5a - c for a southeast Greenland outlet glacier, where velocity from PROMICE v2026 (Fig. 5a), v2021 (Fig. 5b), and a Sentinel-2 image from the same period (Fig. 5c) are compared. The v2021 velocity field is visibly narrower than both the updated product and the optical imagery. This difference arises from the lower spatial resolution of v2021 and from the implementation of an adaptive correlation template size in the updated product (Sec. 5.1), which improves delineation of glacier flow margins. The mean velocity profile across the flux gate indicated in Fig. 5a and b for the year 2021 (Fig. 5d) is both faster and wider in the updated product compared to v2021, demonstrating that the issue was systematic for this glacier. Similar patterns have been observed at other outlet glaciers terminating in relatively narrow fjords particularly along the southeast coast of the GrIS. Changing from v2021 to v2026 of the PROMICE Product has resulted in a 10 % increase in ice flow across the ice flux gates defined in the PROMICE Solid Ice Discharge product (described in Mankoff et al., 2020) in the southeast sector of GrIS.

7.2 Differences in Error Estimates Between v2021 and v2026

A Greenland-wide view of the relative error estimates for the PROMICE product v2026 is shown in Fig. 6 for mosaics from 2020 (approximately one per month). This figure corresponds to Fig. 9 in Solgaard et al. (2021) and presents relative uncer-

https://doi.org/10.5194/essd-2026-221
Preprint. Discussion started: 13 May 2026

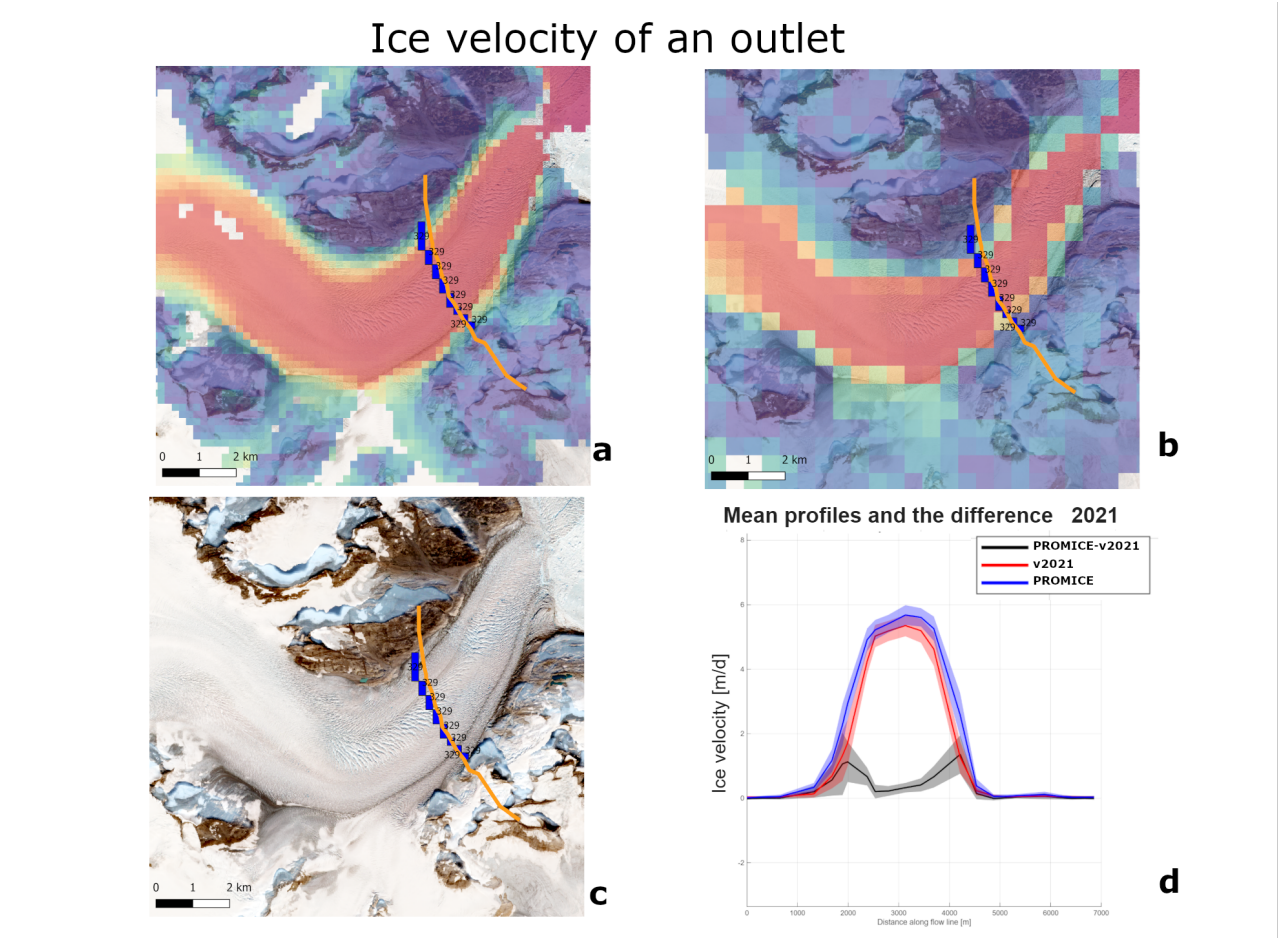

Figure 5. Effect of the implementation of adaptive correlation template sizes and increased resolution. Orange and blue lines show the location of a flux gate across the glacier. Surface velocity magnitude for the period 2021-08-29 to 2021-09-22 from the PROMICE ice velocity dataset v2026 (a) and v2021 (b) with the color scale following the same style as in Fig. 1. Coinciding Copernicus Sentinel-2 imagery from 2021-09-05 Copernicus Sentinel data (2021) is shown in (c) for reference. Mean velocities across the fluxgate for this period from both dataset versions are plotted in (d), where v2026 is plotted in blue, v2021 is plotted in red, and the standard deviation of the difference for the same period is plotted in black.

tainties for the same time periods, but using v2026 data. The reported error estimates are higher in v2026 than in v2021, as is evident when comparing the spatial patterns in Fig. 6 to Fig. 9 in Solgaard et al. (2021). The temporal evolution of the reported error of v2026 and v2021 shown in Fig. 7f shows the same. This is due to the increased spatial resolution of the v2026 product resulting from the introduction of adaptive correlation template sizes (Sec. 5.1). In the v2026 version, a 128×32 correlation template size is initially used in the offset-tracking for a given grid point, and only if this fails, the template size is increased to 256×64 pixels. Where the smaller template size is used, the local standard deviation of the offset estimates, on which the error

https://doi.org/10.5194/essd-2026-221
Preprint. Discussion started: 13 May 2026

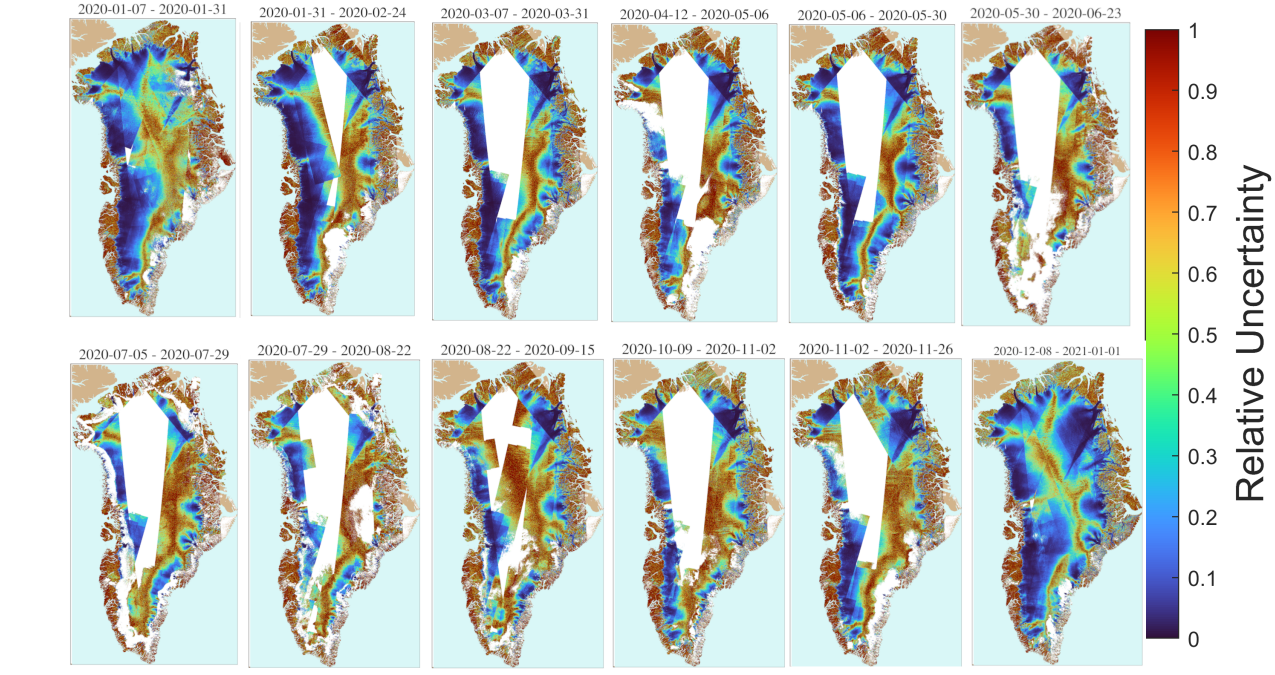

Figure 6. Greenland-wide view of the error estimates for PROMICE v2026 mosaics during 2020. This figure is equivalent to Fig. 9 in Solgaard et al. (2021), but is based on PROMICE v2026 data. Each map shows the reported uncertainty relative to the magnitude of velocity.

estimate is based, increases due to the decreased spatial averaging implied. This was verified by generating a version of the v2026 product using a fixed 256×64 correlation template size (as used in v2021), which resulted in a distribution of reported error estimates nearly identical to the v2021 version.

7.3 Spatial and Temporal Coverage

The spatial coverage of the product varies over time and is influenced by several factors. In general, a higher number of acquisitions over a given grid point increases the likelihood of forming a pair with good coherence. The number of acquisitions itself depends on the time of year, geographic location, and the temporal span of the product.

Temporal coverage also depends on how often coherence is lost, leading to how often the processing fails, as well as on how the properties of the ice-sheet surface have changed between acquisitions (Sect. 5.3 and Sect. 6). These effects, along with the impact of culling, are examined in Figs. 7 and 8.

The updated processing scheme applies stricter outlier removal at the shift map level compared to v2021, resulting in fewer outliers removed during the subsequent image pair culling step (Fig. 7a and b). Consequently, v2026 exhibits lower spatial coverage than v2021, mainly during summer months, even before applying the culling scheme described in Section 5.4. This is illustrated in Figures 7a–d for an individual summer 2018 mosaic and as a time series in Figure 7e, where coverage is defined as the fraction of ice-sheet grid points containing ice velocity data in a given mosaic, such that a value of 1 indicates complete

https://doi.org/10.5194/essd-2026-221
Preprint. Discussion started: 13 May 2026

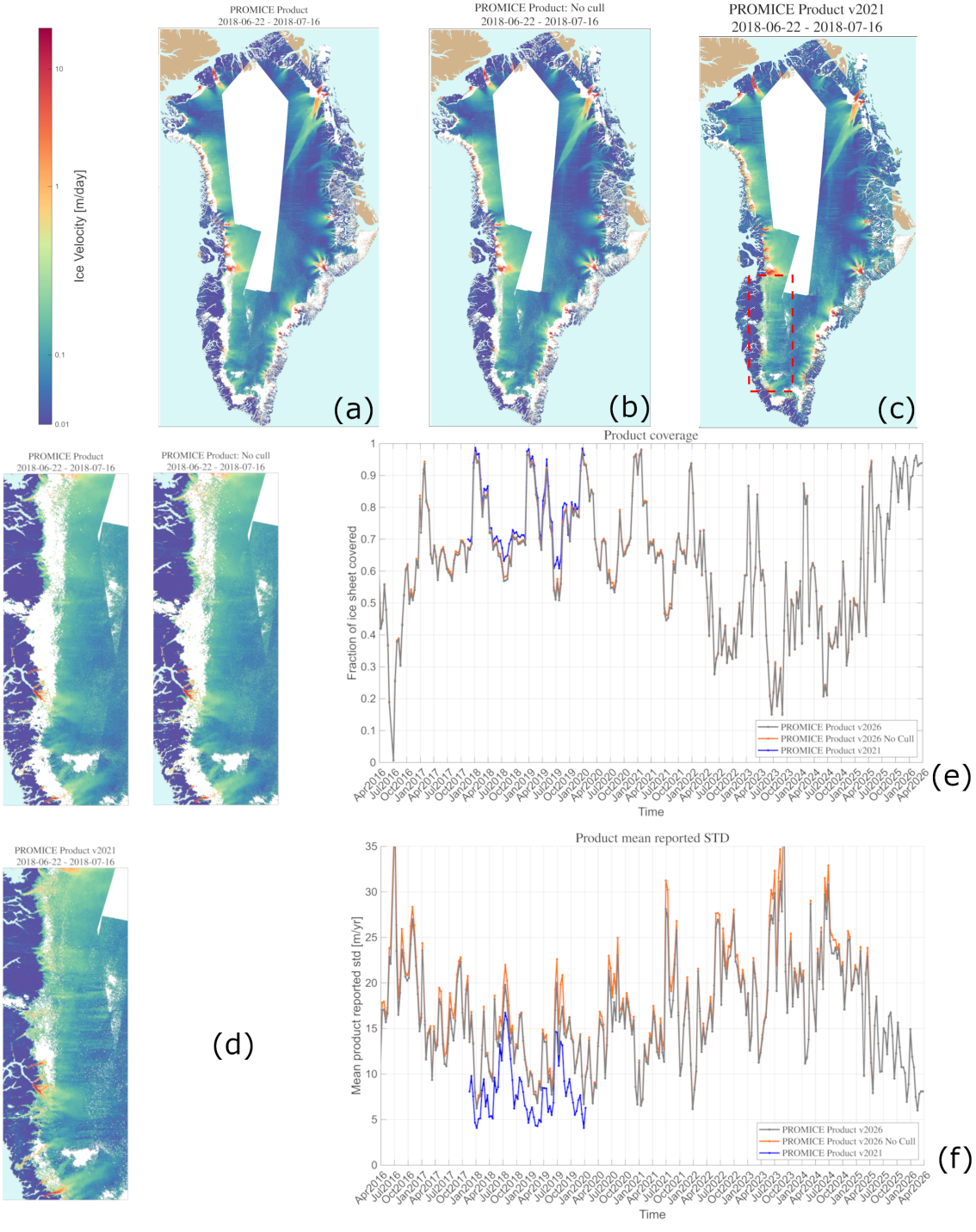

Figure 7. The effect of the culling procedure on the GrIS scale for a map from summer 2018: a) The PROMICE Product v2026. b) The same ice velocity map, but no culling. c) Map from v2021 covering the same period. d) Zoom-in on the red box in western Greenland for each map a)-c). e) Timeseries of product coverage. f) Timeseries of the mean reported (the estimated not the actual) standard deviation for each map.

https://doi.org/10.5194/essd-2026-221
Preprint. Discussion started: 13 May 2026

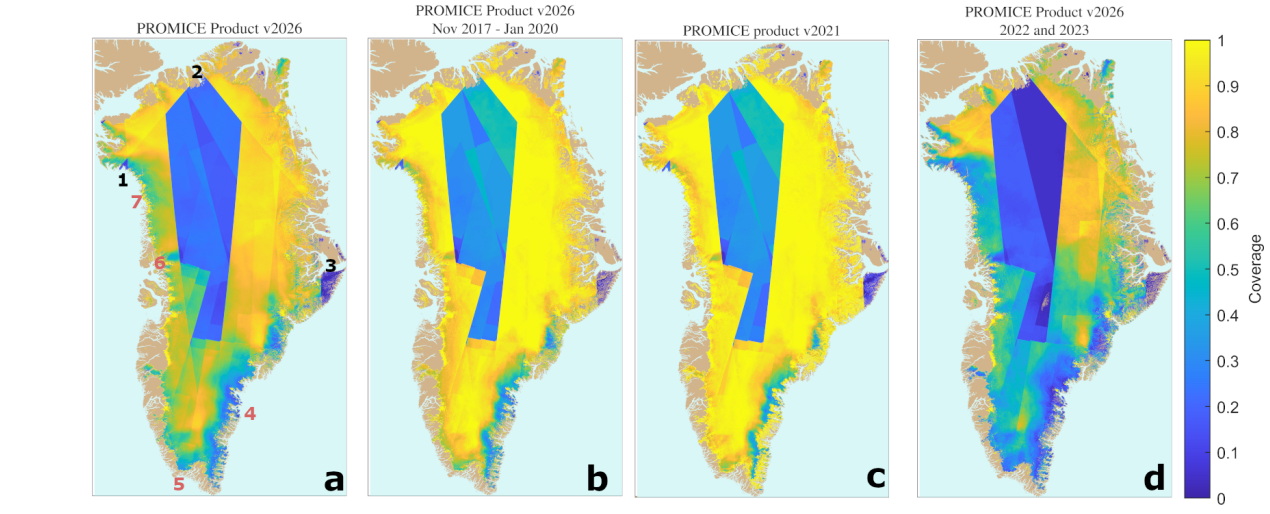

Figure 8. Temporal coverage: Spatial view of the percentage of all mosaics in that have data in a given grid point: a) The PROMICE ice velocity product (v2026), b) the PROMICE Product v2026 for the period 20171106-20200107 c) v2021 for the period 20171106-20200107 and d) the PROMICE Product v2026 spanning 2022 and 2023. The numbers in a) indicate the locations of the areas mentioned in Sec. 7: Areas where SAR in IW mode has not been acquired on a regular basis: 1, 2 and 3 refer to the triangular area in Melville Bay, north Greenland and the Scoresbysund area, respectively. Areas with low ice velocity coverage: 4, 5, 6 and 7 refer to the southeast ice sheet margin, small area in South Greenland, an area north of Rink Glacier and the Melville Bay area, respectively.

coverage. The zoom-in on the southwestern part of the ice sheet reveals that coverage near the margin is lower in v2026 than in v2021 even prior to culling, while noise is reduced in the slower-moving areas closer to the interior.

Both the v2026 and v2021 time series have near-full coverage during peak winter, where winter campaigns ensure full IW coverage of the ice sheet over a number of cycles (Fig. 7e). For v2026 that extends to present day, there is a significant drop in coverage starting in 2022 which is also evident during winter periods. This is the period when the data is based only on 12 day pairs due to the Sentinel-1B malfunction. Coverage goes back up and product reported standard deviation goes down in Spring 2025 where S1-C data became available and the product again is based on data from two satellites. The impact of the period with only one satellite is also evident when comparing Fig. 8a,b and d. The spatial coverage of the PROMICE product v2026 for the period January 2016 - October 2024 (Fig. 8a) is notably lower than Fig. 8 b spanning only November 2017 - January 2020, where Sentinel-1B was fully functional. The largest differences are found along the margins in West, South and Southeast Greenland. Spatial coverage during the period with only one satellite (Fig. 8 d) is clearly reduced.

Figure 8b and c shows the spatial coverage for v2026 and v2021 over the period November 2017 to January 2020. While both versions exhibit similar temporal patterns, Figure 7f demonstrates that v2026 has slightly lower overall coverage, with a pronounced seasonal increase during summer months independent of additional culling.

https://doi.org/10.5194/essd-2026-221
Preprint. Discussion started: 13 May 2026

Both v2026 and v2021 have a large low-coverage area in the ice-sheet interior, where SAR data in IW mode is rarely acquired as is evident from Fig. 2a and 2b. The same explanation goes for the smaller triangular areas in the Melville Bay area, northern Greenland, and the area around Scoresbysund (locations 1, 2, and 3 in Fig. 8a). In the future, we expect better coverage in the interior based on the current acquisition scenario (Fig. 2c). However, the large area with low coverage along the southeast ice sheet margin, an area in southern Greenland, one north of Rink Glacier in west Greenland, and one in the Melville Bay area all have routine SAR IW acquisitions every 6 days (locations 4, 5, 6, and 7 in Fig. 8a). These largely coincide with the regions identified as high accumulation percolation areas (HAPA) by Vandecrux et al. (2019) based on firn properties. HAPAs are areas on the ice sheet characterized by frequent precipitation events and surface melt-water that percolates into the firn -both processes leading to loss of coherence.

8 Validation

We validate the PROMICE ice velocity product against in-situ GNSS measurements from the GrIS and perform an additional analysis over stable ground. Suitable GNSS observations must overlap in time with the period of the PROMICE ice velocity product and have a temporal resolution comparable to or higher than the PROMICE ice velocity product. This limits the number of GNSS measurements available for validation, as most are acquired for purposes other than satellite ice-velocity validation. In contrast to Solgaard et al. (2021), we include observations from other projects in the validation, which we detail below, in addition to PROMICE | GC-Net AWS GNSS observations. This aids the geographical spread and, importantly, adds points with higher velocities compared to the previous validation. The addition of new datasets and the longer time series leads to a substantial increase in the number of validation points: from 695 in Solgaard et al. (2021) to 3370 in this version. Locations and lengths of the GNSS data time series are displayed in Fig. 9. The different sources are described below.

8.1 Sources of GNSS data:

The GNSS validation data were provided with at least daily values of position, which were translated into x- and y-components. The exception is data from the stations at Helheim Glacier (HLM) and at Paakitsoq (Mejia et al., 2020, 2021, 2022, 2025), which were already provided as velocity. We consider data from the following areas in the validation:

Upstream of Sermeq Kujalleq (Jakobshavn Isbræ) [stations with T and cd prefix]: Daily velocity values were estimated from 11 GNSS stations upstream of Sermeq Kujalleq (Jakobshavn Isbræ). Each station logged positions at a 30-second sampling interval using Javad GPS receivers and antennae mounted approximately 2 m above the snow surface. The data time span ranges from a few days to over 400 days, and six sites exceed 100 days of coverage, despite intermittent data loss. Positions were processed in kinematic mode using GIPSY OASIS with JPL final orbits, clocks, and Earth orientation products, applying antenna phase center corrections and following workflows described in Khan et al. (2022) and Christmann et al. (2021). Tropospheric delays were modeled using the Vienna Mapping Function 1 (VMF1) (Boehm et al., 2006), and ocean tide loading corrections were applied via the Automatic Loading Provider using the FES2014b model, including center of mass adjustments. Coordinates are reported in EPSG:3413 (polar stereographic). Plate motion (13–16 mm/yr) was not corrected because

https://doi.org/10.5194/essd-2026-221
Preprint. Discussion started: 13 May 2026

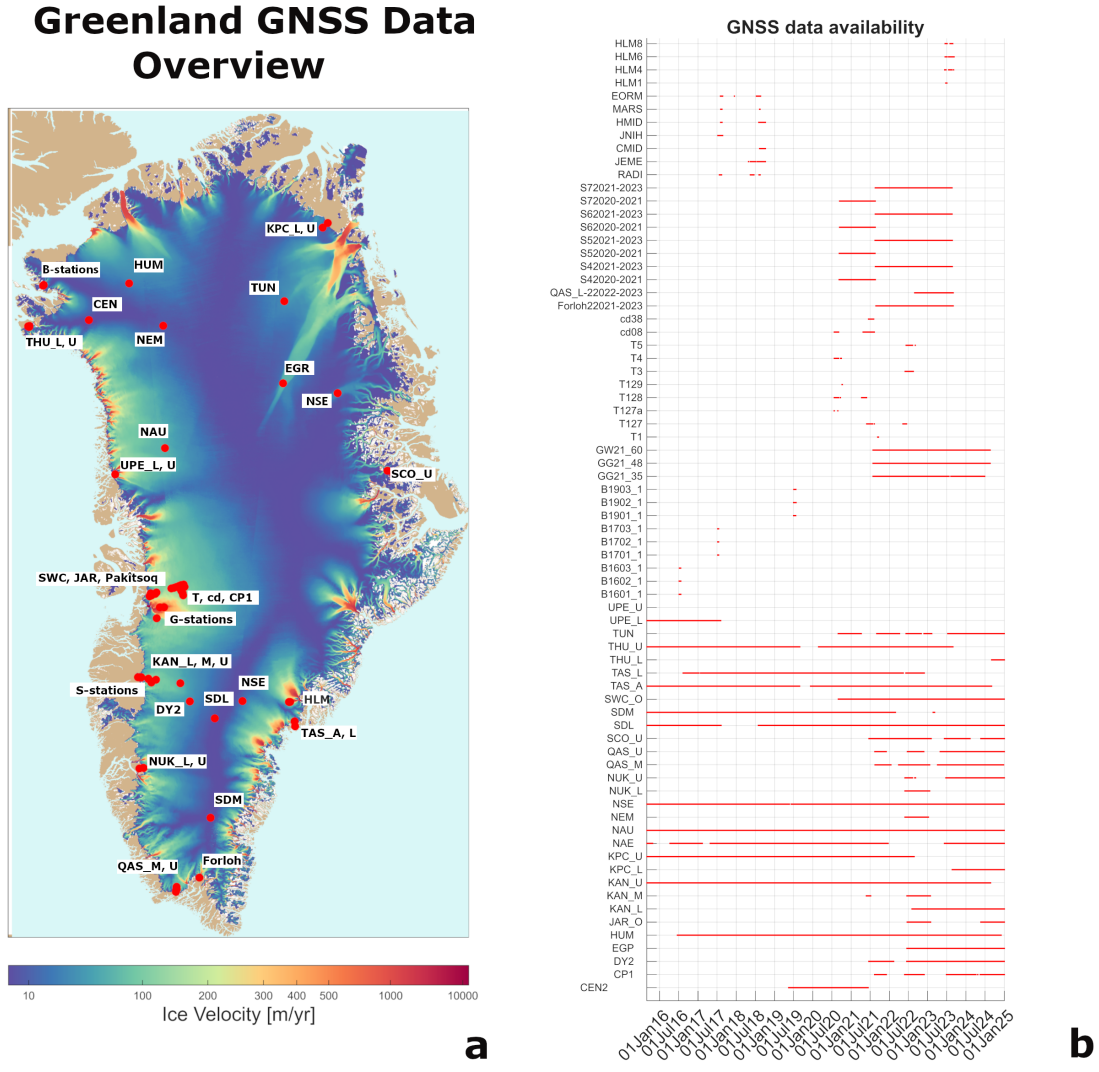

Figure 9. Overview of GNSS data used for validation: a) Locations of the GNSS stations on the GrIS. The ice velocity mosaic used as base layer is a 3 year average of all the PROMICE ice velocity maps spanning September 2016 to September 2019. b) List of GNSS stations used in the validation and their temporal coverage.

it is negligible relative to the ice flow. The observed easting and northing velocity components were determined for each site, as the gradient of the line of best fit of the position-time plots

West and South Greenland [stations S4, S5, S6, S7 and Forloh 2]: GNSS sites S4, S5, S6, S7 and Forloh 2 were equipped with Draw Wire Ice Ablation Trackers (DWIATs) that activate their single-frequency GPS antenna every 2 hours. After their five-minute activation time, the instruments record the median of 50+ GPS measurements, as well as the coordinates for which the lowest HDOP is reported. DWIATs make use of tripods, ,meaning that they move down with a melting surface.

https://doi.org/10.5194/essd-2026-221
Preprint. Discussion started: 13 May 2026

Data from Sermeq Kujalleq (Jakobshavn Isbræ) [stations with G prefix]: Three years of 2-hourly data from three stations along the central flow line of Sermeq Kujalleq (Jakobshavn Isbræ) (Wehrlé et al., 2025).

GNSS data from the Paakitsoq region [stations EORM, MARS, HMID, JNIH, CMID, JEME, RADI]: GNSS validation data was received from seven on-ice GNSS stations deployed in the Paakitsoq ablation area (792—973 m asl and 22-23 km inland from the terminus) summer 2017 and summer 2018 (Mejia et al., 2020, 2021, 2022). GNSS stations were equipped with Trimble Net-R9 receivers and recorded positions at 30 s intervals and were processed using MIT's GAMIT software and bedrock-mounted base stations with baseline lengths between 27 and 37 km. Horizontal ice velocity was then calculated at three-minute intervals following the procedure described in Mejia et al. (2021).

GNSS data from the Helheim Glacier [stations with HLM prefix]: GNSS validation data were received from six on-ice GNSS stations (stations with HLM prefix) deployed in a 4 km region of the accumulation area (1500 m asl) of Helheim Glacier in summer 2023 (Mejia et al., 2025). Similar to the Paakitsoq region, GNSS stations were equipped with Trimble Net-R9 receivers recording positions at 30 s intervals and were processed using GAMIT software utilizing the bedrock-mounted station HEL2 with a baseline length of approximately 38-42 km. Horizontal ice velocity was calculated at three-minute intervals following the procedure described in Mejia et al. (2021).

GPS data from Kangerluarsuup Sermia (Bowdoin Glacier) [stations with B prefix]: Position data is provided every 15 minutes at three stations 4 km upstream from the ice front of Kangerluarsuup Sermia (Bowdoin Glacier) in northwestern Greenland (Sugiyama et al., 2025, 2024). Aluminium poles drilled into the ice were surveyed with GPS receivers running continuously to record L1 and L2 signals every second. The GPS data was processed in a static mode with data from a reference station installed on the glacier flank. The uncertainty in the positioning is expected to be of the order of several millimeters in the horizontal direction, according to the baseline length of < 3 km. We used 10–21-day observations from July 2016, 2017, and 2019 for validation.

PROMICE and GC-Net: PROMICE and GC-Net AWSs measure a range of surface mass-balance components in both the ablation and accumulation zone of the GrIS. The stations are, per design, located in slow-moving areas with average flow generally below 100 m/yr (Fig. 9). The position of the AWS is measured every hour using a single frequency GPS receiver and a small ceramic patch active antenna. We use the freely available hourly positions (How et al., 2022) to calculate velocities. Observations from the GC-Net stations were not included in the previous analysis (Solgaard et al., 2021), and including them increases the number of validation points.

In order to obtain velocities over the same period as each individual satellite product, we use a workflow similar to that described in GIScci-Consortium (2018): Daily positions of the GNSS stations are calculated as the mean of the positions for each day. The velocity components are estimated using a weighted linear regression for each of the 24-day time spans in the velocity mosaics, based on the daily positions. The weights are inversely proportional to the number of measurements used to estimate a daily position, to account for gaps in the data.

Scatter plots of the satellite-derived PROMICE ice velocity product (magnitude, v_x and v_y components) vs. GNSS-derived ice velocities are displayed in Fig. 10. The standard deviation of the difference between the GNSS measurements and the satellite-derived velocity (from here on referred to as the standard deviation) is calculated along with the mean difference

https://doi.org/10.5194/essd-2026-221
Preprint. Discussion started: 13 May 2026

Table 2. Statistics of the validation of the ice velocity product against GNSS data. Top row: Results for validating the entire PROMICE product time series against all the GNSS observations listed in Fig. 9. In order to compare v2026 performance to v2021, we perform a validation over the period used in Solgaard et al. (2021) Tab. 5 (20171106-20200106) and use the same PROMICE AWS stations: (EGR, KAN_L,KAN_M, KAN_U, KPC_L, NUK_L, NUK_U, QAS_M, QAS_U, TAS_A, TAS_L, THU_L, THU_U, UPE_L and UPE_U) (Solgaard et al. (2021) Fig. 12): Middle: Results for v2021 and Bottom: Results for v2026.

Product	Magnitude		x-dir		y-dir	
	Mean difference [m/yr]	Std of mean diff [m/yr]	Mean diff [m/yr]	Std of mean diff [m/yr]	Mean diff [m/yr]	Std of mean diff [m/yr]
PROMICE Product v2026	-0.3	23	-1	22	-0.4	38
PROMICE Product v2021 [Nov 2017 - Jan 2020]	4	19	-3	20	-1	27
PROMICE Product v2026 [Nov 2017 - Jan 2020]	1	19	-0.2	17	1	28

(bias) between GNSS and satellite velocity (see first line in Table 2). These values reflect not only the uncertainty of the satellite-derived product but also that of the GNSS-derived velocity, and note also that this standard deviation is not the same as the standard deviation reported as part of the product (see Sect. 6). The expected error of the satellite product is estimated to be 10-30 m/yr for individual pairs (GIScci-Consortium, 2013).

We perform the validation both for the entire time series up to October 2024 as well as for the subset November 2017 - January 2020. The latter is carried out to compare statistics with v2021, which was done during this period in Solgaard et al. (2021). It is also a period during which data are available from two satellites. For the entire period, mean differences are < 1 m/yr and a standard deviation of the difference ranging from 22 m/yr for the v_x-component and 38 m/yr for the v_y-component. The larger standard deviation for the v_y component is expected: Due to the general north-south orientation of the satellite tracks (Fig. 2), the v_y-component is aligned roughly parallel to the azimuth direction (satellite flight path), and Sentinel-1 IW SLC images (see Sect. 4.1) have a much lower resolution in azimuth than in the range (line-of-)sight direction). We note that due to the roughly east/west orientation of most Greenland glaciers, the velocity range of the y-component in our validation is notably smaller than that of the x-component.

Comparison to v2021 shows a reduction in the bias and standard deviation for the v_x-component and similar values for the v_y-component. The higher values of the bias and standard deviation for the entire period, compared to the subset, mainly stem from the one-satellite period and the new validation dataset, which includes areas with higher velocities. Figure. 10 b shows for the x-component an increase in deviations at higher absolute velocity values and similarly for the y-component. If these points were excluded, the statistics would become very similar to the subset values. It is not possible to conclude whether deviations between GNSS observations and the PROMICE product are generally larger for faster flow, given the low number of validation points in this study. GNSS observations from areas with faster flow are clearly underrepresented in this validation.

https://doi.org/10.5194/essd-2026-221
Preprint. Discussion started: 13 May 2026

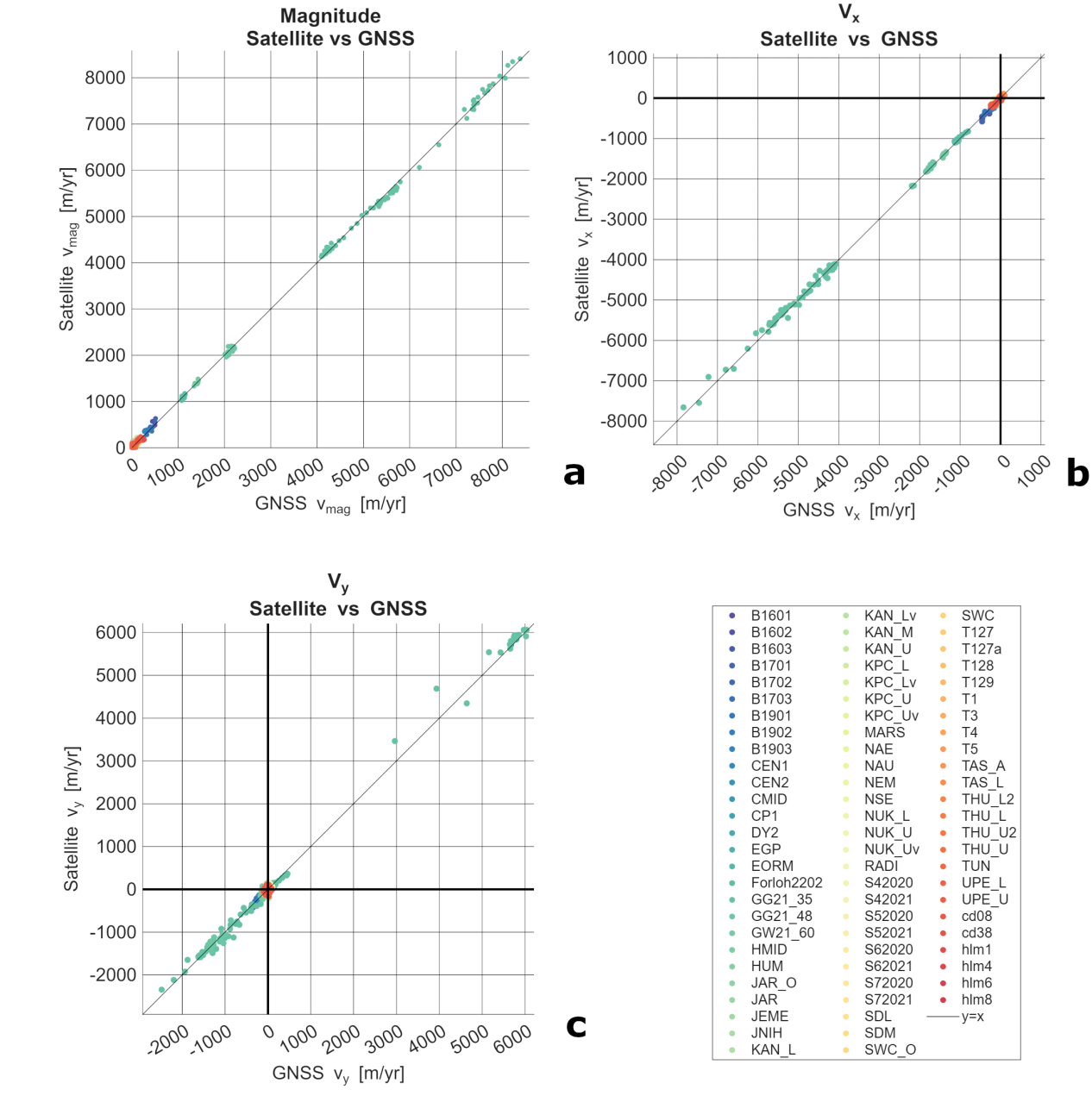

Figure 10. Scatter plots of GNSS derived ice velocity vs PROMICE ice velocity. a): Scatter plot of the magnitude of the velocity. b): Scatter plot of the v_x-component. c): Scatter plot of the v_y-component

https://doi.org/10.5194/essd-2026-221
Preprint. Discussion started: 13 May 2026

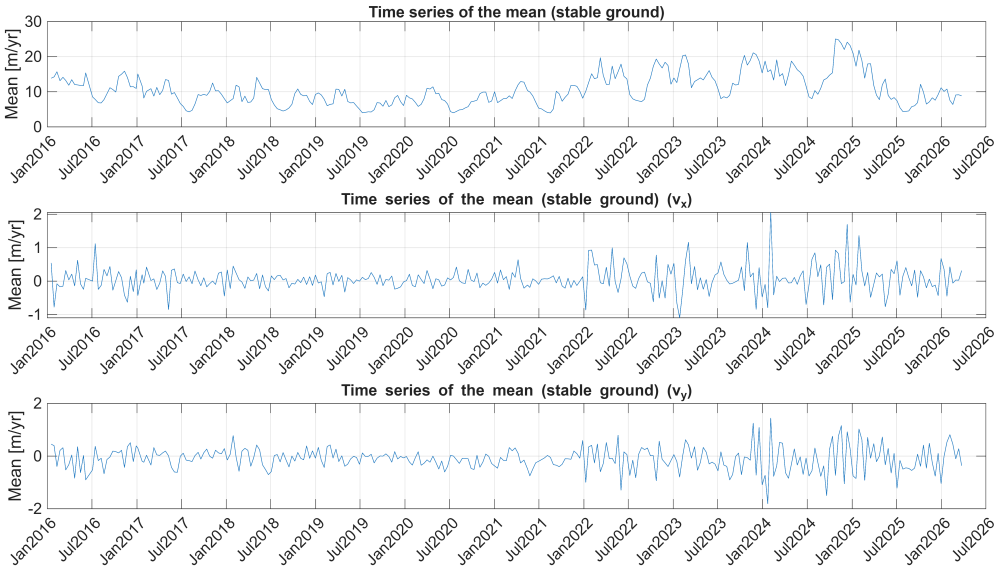

Figure 11. Time series of the mean of the PROMICE Product over stable ground, where no movement is expected.

We perform a similar analysis for the PROMICE product for the pixels over stable ground, where no movement is expected. All pixels on ice-free terrain from all mosaics (each spanning 24 days) in the time series are included, which totals to $\approx 2 \cdot 10^9$ pixels. The resulting values of the bias and the standard deviation of the difference are 0.1 m/yr and 7 m/yr for the v_x-component and -0.1 m/yr and 12 m/yr for the v_y-component, respectively (see Table 3). The standard deviations for the stable ground validations are substantially lower than the standard deviations obtained through validation against GNSS measurements (less than half), and the bias for each component is lower (in absolute value) and thus closer to zero as well. In this analysis, the standard deviation is also largest for the v_y-component for the same reasons as discussed above. Table 3 also provides statistics from the validation against GNSS for both the v2026 and v2021 versions of the product during an identical time span (November 2017 - January 2020). It shows that v2026 performs slightly better with reduced standard deviations for both velocity components. The v2026 product also performs better for the subset period, during which two satellites provide data, compared to the entire ice velocity time series. The time series of the mean difference over stable ground for the magnitude and each component is displayed in Fig. 11. Here it is also clear that the standard deviation suddenly increases at the end of 2021, where Sentinel-1B data is no longer available.

The uncertainty observed over stable ground (Fig. 11) is lower than that obtained from validation against GNSS observations (Table 2 and Fig. 7). This discrepancy is partly explained by uncertainties in the GNSS-derived velocity estimates themselves.

The reported uncertainty of v2026 is higher than that of v2021, but remains lower than—or comparable to—the uncertainty observed during validation against GNSS measurements and over stable ground when compared with v2021. Some sources of error are inherent to the data and cannot be fully accounted for by the algorithm. This is especially true for the spatially

https://doi.org/10.5194/essd-2026-221
Preprint. Discussion started: 13 May 2026

Table 3. Statistics of the validation of the PROMICE product (spanning 24 days) over stable ground. Number of pixels included in the analysis: $2 \cdot 10^9$.

Product	Magnitude		x-dir		y-dir	
	Mean difference [m/yr]	Std of mean diff [m/yr]	Mean diff [m/yr]	Std of mean diff [m/yr]	Mean diff [m/yr]	Std of mean diff [m/yr]
PROMICE Product v2026	11	13	0.1	9	-0.1	15
No Cull	12	23	0.1	14	-0.1	22
PROMICE Product V2021 [Nov 2017 - Jan 2020]	10	10	0.1	8	-0.6	12
Promice Product v2026 [Nov 2017 - Jan 2020]	8	11	0	7	0	11

correlated errors caused by ionospheric scintillations (Sect. 6.1), which are not fully estimated by the error estimation algorithm. The difference between v2021 and v2026 reported uncertainties is explained in Sec. 7.2. For a time series of mosaics like the PROMICE ice velocity product, errors will vary both spatially and temporally due to the sources described in Sect. 6 as well as to variations in data coverage (Sect. 5.3 and Fig. 2a).

The current collection of validation data is an improvement over the one applied in v2021, but it is still biased towards slow-flowing areas. An ideal validation data set is representative of a larger range of flow regimes, gradients in the flow field, and surface conditions would help assess whether the reported product errors are captured correctly and thus ultimately help improve product performance. The analysis above, however, shows that the size of the product errors is as expected.

9 Living Data: Updates and Improvements

PROMICE will continue to distribute and update the PROMICE Ice Velocity product based on the Sentinel-1 data collected and released by ESA and the Copernicus programme. We aim to deliver a clean, homogeneous data product that is updated regularly, with a new mosaic released every 12 days, while provide the possibility for user interaction and issue resolution. Associated with PROMICE, we have a user-contributable dynamic web-based data archive (GitHub), which lists known data quality issues [https://github.com/GEUS-PROMICE/Sentinel-1_Greenland_Ice_Velocity]. On the GitHub page, we also allow data users to report and document new issues. Documenting dataset issues is often simpler than correcting them, and future dataset versions will implement fixes to any verified issues as soon as they are done. All fixed issues will be tagged as closed and remain visible for new users.

To improve accessibility, the dataset is now available via a THREDDS Data Server (https://thredds.geus.dk/thredds/catalog/catalogs/ivdata.html), which provides access through the OPeNDAP protocol enabling subsetting by spatial region (region of interest, ROI) and time range. This eliminates the need for downloading full data files for many use cases. Multiple Jupyter Notebooks are available at https://github.com/GEUS-PROMICE/Sentinel-1_Greenland_Ice_Velocity for quick hands-on tuto-

https://doi.org/10.5194/essd-2026-221
Preprint. Discussion started: 13 May 2026

rials. These notebooks provide code examples of how to download data, extract a flow line, a point or an area from a data file or a time series of data files

We encourage users working with Sentinel-1 and PROMICE ice-velocity data to search the issue database to see whether there are any known data issues relevant to their needs. We find it likely that there are unknown issues in the existing data, and that new issues may arise in the future data collection pipeline. We aim to continue improving the dataset by incorporating user input through the GitHub page.

10 Summary and Outlook

The PROMICE ice velocity product is a time series of Greenland ice sheet wide ice velocity mosaics based on offset-tracking of Sentinel-1 images 6 and 12 days apart. The resulting velocity maps from all image pairs acquired during a 24-day period are temporally averaged and mosaicked to produce a consistent coverage. A new mosaic is produced every 12 days and aimed to be made available within 10 days of the last included acquisition. In this paper, focus is on the updates to the processing chain relative to Solgaard et al. (2021), and we refer to that paper for details not included here. We discuss the differences and improvements between v2026 and v2021, and explore the impact of the period with only one functioning satellite on product quality:

The spatial posting of the product has been refined from a 500 m to a 200 m grid justified by the implementation of an adaptive correlation template size, when performing the cross correlation. This new feature in the processing also leads to better delineation of flow and helps resolve the episodes of artificial slow downs, where the larger template failed at a number of outlets particularly in Southeast Greenland found in the previous version of the dataset. Noise stemming from ionospheric effects has also been reduced at the locations of crossing tracks due to the implementation of a new method for producing mosaics. Reported error estimates in the v2026 products are higher than in v2021, due to the increased spatial resolution introduced by the adaptive correlation template size.

Similarly to Solgaard et al. (2021), the PROMICE ice velocity product v2026 was validated against GNSS observations. In order to improve this validation, several new datasets were included and lead to an increase in validation points from 695 in Solgaard et al. (2021) to 3370 in this version. The addition of datasets provides a better geographical coverage and provides observations from areas with higher velocity. Despite these additions, the validation dataset is still skewed towards slow moving areas and could be improved by having a better representation of the range of flow regimes, gradients and surface conditions.

Validation against the observations from GNSS shows that the standard deviation of the difference between the ice velocity product and the GNSS data is 17 m/yr and 28 m/yr for v_x and v_y-component, respectively. This is within the expected uncertainty range of 10-30 m/yr (GIScci-Consortium, 2013). However, we expect the actual values pertaining to the PROMICE ice velocity product to be lower as the GNSS data carries a non-negligible part of the uncertainty. This is indicated by the analysis carried out for pixels over stable ground, which show a standard deviation of 9 m/yr and 15 m/yr for v_x and v_y-component, respectively, in line with the findings of Hvidberg et al. (2020). Better spatially distributed validation data with low uncertainty would help assess whether the processor captures the spatially and temporally varying uncertainty field correctly.

https://doi.org/10.5194/essd-2026-221
Preprint. Discussion started: 13 May 2026

The values reported from the validation of the current version of PROMICE ice velocity product are higher than what we reported in Solgaard et al. (2021). This stems from the longer validation period which includes the period where only S1-A was operational. Our analyses show a clear increase in product noise accompanied by a reduction in spatial coverage in the period between the failure of S1-B and the commissioning of S1-C.

Product coverage also varies temporally and spatially in response to changes in SAR acquisition patterns and seasonal variations in surface properties. Coverage is distinctly lower during the period with only one operational Sentinel-1 satellite. The southeast GrIS margin has good Sentinel-1 SAR data coverage but often has gaps in the mosaics due to surface property changes caused by surface melt and high precipitation rates, which hinder velocity retrieval. Other areas, like the small triangular area in the Melville Bay area, have low coverage in the mosaics simply due to a lack of SAR data.

The PROMICE Ice Velocity product will continue to be updated as long as the Sentinel-1 satellites remain in operation. We will continue to make improvements to the product, and these updates will be posted at https://github.com/GEUS-Glaciology-and-Climate/Sentinel-1_Greenland_Ice_Velocity. We encourage uses to add and document product issues or suggest improvements.

The PROMICE ice velocity product presented here was originally intended primarily to calculate ice discharge through marine-terminating glaciers of the GrIS as done in the PROMICE solid ice discharge product (Mankoff et al., 2020). The PROMICE ice velocity product is thus less suited for studying very short-lived changes in the velocity structure, as observed in-situ by e.g. Bartholomew et al. (2012), Ahlstrøm et al. (2013) and Mejia et al. (2021) or through higher frequency acquisitions/non-mosaic products of satellite imagery as done by e.g. Davison et al. (2020) and Larsen et al. (2023). By not mosaicking all individual image pairs, as we do for the PROMICE ice velocity product, much higher temporal resolution over a limited region is possible with datasets such as the ITS_LIVEproduct (Gardner et al., 2025). Yet, the spatially comprehensive and temporally consistent nature of the PROMICE ice velocity product makes it attractive for longer-term large-scale monitoring of the GrIS velocity structure and glacier dynamics as done by Vijay et al. (2019), Solgaard et al. (2022), Khan et al. (2022) and Grinsted et al. (2024).

11 Data availability

The PROMICE Ice Velocity product (DOI: https://doi.org/10.22008/FK2/K70OPK, (Solgaard and Kusk, 2026)) is publicly available through the Dataverse repository hosted by GEUS (https://dataverse.geus.dk/dataverse/Ice_velocity), which serves as the authoritative, DOI-resolving archive and provides access to the complete data files. In addition, the GEUS THREDDS data server (https://thredds.geus.dk/thredds/catalog/catalogs/ivdata.html) offers programmatic access via the OPeNDAP protocol, enabling subsetting by spatial region (region of interest, ROI) and time range.

https://doi.org/10.5194/essd-2026-221
Preprint. Discussion started: 13 May 2026

Open Access Earth System Science Data Discussions

Author contributions. AS and AK designed and produced the PROMICE ice velocity product. AK, JPMB and JD developed the processing software. RSF, MCL and KDM set up the data-curation framework. PH designed the Jupyter Notebook tutorials. AS and AK prepared the manuscript with contributions from all co-authors.

Competing interests. KDM is an ESSD editor.

Acknowledgements. Ice velocity maps were produced as part of the Programme for Monitoring of the Greenland Ice Sheet (PROMICE) using Copernicus Sentinel-1 SAR images distributed by ESA, and were provided by the Geological Survey of Denmark and Greenland (GEUS) at http://www.promice.dk.

Data from the Programme for Monitoring of the Greenland Ice Sheet (PROMICE) are provided by the Geological Survey of Denmark and Greenland (GEUS) at http://www.promice.dk. ZAC, LYN, FRE and NUK_K stations are financially supported by the Glaciobasis programme as part of the Greenland Ecosystem Monitoring project (https://g-e-m.dk/). The NUK_K station is owned and maintained by Asiaq Greenland Survey. The WEG stations are funded and maintained by Jakob Abermann at the Department of Geography and Regional Science of the University of Graz. The RED_L station is funded and maintained by Rainer Prinz at the Department of Atmospheric and Cryospheric Sciences of the University of Innsbruck. The NUK_B station is funded and maintained by James Lea at the University of Liverpool. The SER_B station is funded and maintained by Anders Bjørk at the Department of Geosciences and Natural Resource Management of the University of Copenhagen.

Grounding line data are provided by the ESA Greenland Ice Sheet CCI project (www.esa-icesheets-greenland-cci.org). Ken Mankoff was supported by the NASA Modeling Analysis and Prediction program.

https://doi.org/10.5194/essd-2026-221
Preprint. Discussion started: 13 May 2026

References

Ahlstrøm, A. P., Andersen, S. B., Andersen, M. L., Machguth, H., Nick, F. M., Joughin, I., Reijmer, C. H., van de Wal, R. S. W., Merryman Boncori, J. P., Box, J. E., Citterio, M., van As, D., Fausto, R. S., and Hubbard, A.: Seasonal velocities of eight major marine-terminating outlet glaciers of the Greenland ice sheet from continuous in situ GPS instruments, Earth System Science Data, 5, 277–287, https://doi.org/10.5194/essd-5-277-2013, 2013.

Andersen, J., Kusk, A., Boncori, J., Hvidberg, C., and Grinsted, A.: Improved ice velocity measurements with Sentinel-1 TOPS interferometry, Remote Sensing, 12, https://doi.org/10.3390/rs12122014, 2020.

Andersen, J. K., Meyer, R. P., Huiban, F. S., Dømgaard, M. L., Millan, R., and Bjørk, A. A.: Brief communication: Storstrømmen Glacier, northeastern Greenland, primed for end-of-decade surge, The Cryosphere, 19, 1717–1724, https://doi.org/10.5194/tc-19-1717-2025, https://tc.copernicus.org/articles/19/1717/2025/, 2025.

Bartholomew, I., Nienow, P., Sole, A., Mair, D., Cowton, T., and King, M. A.: Short-term variability in Greenland Ice Sheet motion forced by time-varying meltwater drainage: Implications for the relationship between subglacial drainage system behavior and ice velocity, Journal of Geophysical Research: Earth Surface, 117, https://doi.org/https://doi.org/10.1029/2011JF002220, 2012.

Boehm, J., Werl, B., and Schuh, H.: Troposphere mapping functions for GPS and very long baseline interferometry from European Centre for Medium-Range Weather Forecasts operational analysis data, Journal of geophysical research: solid earth, 111, https://doi.org/https://doi.org/10.1029/2005JB003629, 2006.

Boncori, J. P. M., Andersen, M. L., Dall, J., Kusk, A., Kamstra, M., Andersen, S. B., Bechor, N., Bevan, S., Bignami, C., Gourmelen, N., and et al.: Intercomparison and Validation of SAR-Based Ice Velocity Measurement Techniques within the Greenland Ice Sheet CCI Project, Remote Sensing, 10, 929, https://doi.org/10.3390/rs10060929, http://dx.doi.org/10.3390/rs10060929, 2018.

Brough, S., Carr, J. R., Ross, N., and Lea, J. M.: Ocean-Forcing and Glacier-Specific Factors Drive Differing Glacier Response Across the 69°N Boundary, East Greenland, Journal of Geophysical Research: Earth Surface, 128, e2022JF006 857, https://doi.org/https://doi.org/10.1029/2022JF006857, https://agupubs.onlinelibrary.wiley.com/doi/abs/10.1029/2022JF006857, e2022JF006857 2022JF006857, 2023.

Center, S.-. M. P.: Instrument Timing Calibration Product [AUX_ITC], https://sar-mpc.eu/adf/aux_itc/, 2026.

Christmann, J., Helm, V., Khan, S. A., Kleiner, T., Müller, R., Morlighem, M., Neckel, N., Rückamp, M., Steinhage, D., Zeising, O., et al.: Elastic deformation plays a non-negligible role in Greenland's outlet glacier flow, Communications Earth & Environment, 2, 232, https://doi.org/https://doi.org/10.1038/s43247-021-00296-3, 2021.

Copernicus Sentinel data: Sentinel-2 L2A, Processed by ESA, retrieved from the Copernicus Browser, accessed: 05 July 2024, 2021.

Davison, B. J., Sole, A. J., Cowton, T. R., Lea, J. M., Slater, D. A., Fahrner, D., and Nienow, P. W.: Subglacial Drainage Evolution Modulates Seasonal Ice Flow Variability of Three Tidewater Glaciers in Southwest Greenland, Journal of Geophysical Research: Earth Surface, 125, e2019JF005 492, https://doi.org/https://doi.org/10.1029/2019JF005492, 2020.

de Lange, R., Luckman, A., and Murray, T.: Improvement of Satellite Radar Feature Tracking for Ice Velocity Derivation by Spatial Frequency Filtering, IEEE Transactions on Geoscience and Remote Sensing, 45, 2309–2318, https://doi.org/10.1109/TGRS.2007.896615, 2007.

DLR: TanDEM-X - Digital Elevation Model (DEM) - Global, 90m, https://doi.org/https://doi.org/10.15489/ju28hc7pui09, 2018.

Fausto, R. S., How, P., Vandecrux, B., Lund, M. C., Box, J. E., Mankoff, K. D., Andersen, S. B., van As, D., Bahbah, R., Citterio, M., Colgan, W., Jakobsgaard, H. T., Karlsson, N. B., Kjeldsen, K. K., Larsen, S. H., Olsen, C., Oraschewski, F., Rutishauser, A., Shields, C. L.,

https://doi.org/10.5194/essd-2026-221
Preprint. Discussion started: 13 May 2026

Solgaard, A. M., Stevens, I. T., Svendsen, S. H., Langley, K., Messerli, A., Bjørk, A. A., Andersen, J. K., Abermann, J., Steiner, J., Prinz, R., Hynek, B., Lea, J. M., Brough, S., and Ahlstrøm, A. P.: PROMICE | GC-NET automatic weather station data, Earth System Science Data Discussions, 2025, 1–80, https://doi.org/10.5194/essd-2025-687, https://essd.copernicus.org/preprints/essd-2025-687/, 2025.

Gardner, A. S., Fahnestock, M. A., and Scambos, T. A.: ITS_LIVE Regional Glacier and Ice Sheet Surface Velocities., Data archived at National Snow and Ice Data Center, https://doi.org/10.5067/6II6VW8LLWJ7, 2019.

Gardner, A. S., Greene, C. A., Kennedy, J. H., Fahnestock, M. A., Liukis, M., López, L. A., Lei, Y., Scambos, T. A., and Dehecq, A.: ITS_LIVE global glacier velocity data in near-real time, The Cryosphere, 19, 3517–3533, https://doi.org/10.5194/tc-19-3517-2025, https://tc.copernicus.org/articles/19/3517/2025/, 2025.

GIScci-Consortium: Comprehensive Error Characterisation Report for the Greenland Ice Sheet cci project of ESA's Climate Change Initiative, version 1.2, Tech. rep., European Space Agency, 2013.

GIScci-Consortium: Product Validation and Intercomparison Report (PVIR) for the Greenland Ice Sheet cci project of ESA's Climate Change Initiative, version 3.0, Tech. rep., European Space Agency, 2018.

Gray, A. L., Mattar, K. E., and Sofko, G.: Influence of Ionospheric Electron Density Fluctuations on Satellite Radar Interferometry, Geophysical Research Letters, https://doi.org/10.1029/2000GL000016, 2000.

Grinsted, A., Rathmann, N. M., Mottram, R., Solgaard, A. M., Mathiesen, J., and Hvidberg, C. S.: Failure strength of glacier ice inferred from Greenland crevasses, The Cryosphere, 18, 1947–1957, https://doi.org/10.5194/tc-18-1947-2024, https://tc.copernicus.org/articles/18/1947/2024/, 2024.

How, P., Lund, M., Ahlstrøm, A., Andersen, S., Box, J., Citterio, M., Colgan, W., Fausto, R., Karlsson, N., Jakobsen, J., Jakobsgaard, H., Larsen, S., Mankoff, K., Nielsen, R., Rutishauser, A., Shield, C., Solgaard, A., Stevens, I., van As, D., Vandecrux, B., Abermann, J., Bjørk, A., Langley, K., Lea, J., Messerli, A., and Prinz, R.: PROMICE and GC-Net automated weather station data in Greenland, https://doi.org/10.22008/FK2/IW73UU, https://doi.org/10.22008/FK2/IW73UU, 2022.

Howat, I. M., Box, J. E., Ahn, Y., Herrington, A., and McFadden, E. M.: Seasonal variability in the dynamics of marine-terminating outlet glaciers in Greenland, Journal of Glaciology, 56, 601–613, https://doi.org/10.3189/002214310793146232, 2010.

Hvidberg, C. S., Grinsted, A., Dahl-Jensen, D., Khan, S. A., Kusk, A., Andersen, J. K., Neckel, N., Solgaard, A., Karlsson, N. B., Kjær, H. A., and Vallelonga, P.: Surface velocity of the Northeast Greenland Ice Stream (NEGIS): assessment of interior velocities derived from satellite data by GPS, The Cryosphere, 14, 3487–3502, https://doi.org/10.5194/tc-14-3487-2020, 2020.

Joughin, I.: MEaSUREs Greenland Annual Ice Sheet Velocity Mosaics from SAR and Landsat, Version 2., Boulder, Colorado USA. NASA National Snow and Ice Data Center Distributed Active Archive Center., https://doi.org/10.5067/TZZDYD94IMJB, 2020a.

Joughin, I.: MEaSUREs Greenland Monthly Ice Sheet Velocity Mosaics from SAR and Landsat, Version 2., Boulder, Colorado USA. NASA National Snow and Ice Data Center Distributed Active Archive Center., https://doi.org/0.5067/11MJZGPBK3ZF, 2020b.

Joughin, I.: MEaSUREs Greenland Quarterly Ice Sheet Velocity Mosaics from SAR and Landsat, Version 2, Boulder, Colorado USA. NASA National Snow and Ice Data Center Distributed Active Archive Center., https://doi.org/10.5067/3ZMCUIFDYJG4, 2020c.

Joughin, I., Smith, B. E., Howat, I. M., Scambos, T., and Moon, T.: Greenland flow variability from ice-sheet-wide velocity mapping, Journal of Glaciology, 56, 415–430, https://doi.org/10.3189/002214310792447734, 2010.

Joughin, I., Smith, B. E., and Howat, I.: Greenland Ice Mapping Project: ice flow velocity variation at sub-monthly to decadal timescales, The Cryosphere, 12, 2211–2227, https://doi.org/10.5194/tc-12-2211-2018, 2018.

Joughin, L. R., Kwok, R., and Fahnestock, M. A.: Interferometric estimation of three-dimensional ice-flow using ascending and descending passes, IEEE Transactions on Geoscience and Remote Sensing, https://doi.org/10.1109/36.655315, 1998.

https://doi.org/10.5194/essd-2026-221
Preprint. Discussion started: 13 May 2026

Khan, S. A., Choi, Y., Morlighem, M., Rignot, E., Helm, V., Humbert, A., Mouginot, J., Millan, R., Kjær, K. H., and Bjørk, A. A.: Extensive inland thinning and speed-up of Northeast Greenland Ice Stream, Nature, 611, 727–732, https://doi.org/https://doi.org/10.1038/s41586-022-05301-z, 2022.

Khan, S. A., Morlighem, M., Ehrenfeucht, S., Seroussi, H., Choi, Y., Rignot, E., Humbert, A., Pickell, D., and Hassan, J.: Inland Summer Speedup at Zachariæ Isstrøm, Northeast Greenland, Driven by Subglacial Hydrology, Geophysical Research Letters, 51, e2024GL110 691, https://doi.org/https://doi.org/10.1029/2024GL110691, https://agupubs.onlinelibrary.wiley.com/doi/abs/10.1029/2024GL110691, e2024GL110691 2024GL110691, 2024.

Koldtoft, I., Grinsted, A., Vinther, B. M., and Hvidberg, C. S.: Ice thickness and volume of the Renland Ice Cap, East Greenland, Journal of Glaciology, 67, 714–726, https://doi.org/10.1017/jog.2021.11, 2021.

Kusk, A., Boncori, J., and Dall, J.: An automated system for ice velocity measurement from SAR, in: Proceedings of the 12th European Conference on Synthetic Aperture Radar (EUSAR 2018), Proceedings of the European Conference on Synthetic Aperture Radar, pp. 929–932, VDE Verlag, 2018.

Larsen, S. H., Ahlstrøm, A. P., Karlsson, N. B., Kusk, A., Langen, P. L., and Hvidberg, C. S.: Outlet glacier flow response to surface melt: based on analysis of a high-resolution satellite data set, Journal of Glaciology, 69, 1047–1055, https://doi.org/10.1017/jog.2022.124, 2023.

Lewis, J.: Fast Template Matching, in: Vision Interface, vol. 10, pp. 120–123, 1995.

Maier, N., Humphrey, N., Harper, J., and Meierbachtol, T.: Sliding dominates slow-flowing margin regions, Greenland Ice Sheet, Science Advances, 5, https://doi.org/10.1126/sciadv.aaw5406, 2019.

Mankoff, K. D., Solgaard, A., Colgan, W., Ahlstrøm, A. P., Khan, S. A., and Fausto, R. S.: Greenland Ice Sheet solid ice discharge from 1986 through March 2020, Earth System Science Data, 12, 1367–1383, https://doi.org/10.5194/essd-12-1367-2020, 2020.

Mejia, J., Gulley, J., and Dixon, T.: West Greenland moulins 2017–2019 Sermeq Avannarleq—GPS/GNSS observations dataset, 2020.

Mejia, J. Z., Gulley, J. D., Trunz, C., Covington, M. D., Bartholomaus, T. C., Xie, S., and Dixon, T. H.: Isolated Cavities Dominate Greenland Ice Sheet Dynamic Response to Lake Drainage, Geophysical Research Letters, 48, e2021GL094 762, https://doi.org/https://doi.org/10.1029/2021GL094762, https://agupubs.onlinelibrary.wiley.com/doi/abs/10.1029/2021GL094762, e2021GL094762 2021GL094762, 2021.

Mejia, J. Z., Gulley, J. D., Trunz, C., Covington, M. D., Bartholomaus, T. C., Breithaupt, C., Xie, S., and Dixon, T. H.: Moulin Density Controls the Timing of Peak Pressurization Within the Greenland Ice Sheet's Subglacial Drainage System, Geophysical Research Letters, 49, e2022GL100 058, https://doi.org/https://doi.org/10.1029/2022GL100058, 2022.

Mejia, J. Z., Poinar, K., Meyer, C. R., Sommers, A. N., and Chu, W.: Mechanisms for upstream migration of firn aquifer drainage: preliminary observations from Helheim Glacier, Greenland, Journal of Glaciology, 71, e5, https://doi.org/10.1017/jog.2024.78, 2025.

Miranda, N.: Definition of the TOPS SLC deramping function for products generated by the S-1 IPF (Technical Note COPE-GSEG-EOPG-TN-14-0025, Issue 1, Rev. 3), Tech. rep., European Space Agency, 2017.

Moon, T., Joughin, I., Smith, B., van den Broeke, M. R., van de Berg, W. J., Noël, B., and Usher, M.: Distinct patterns of seasonal Greenland glacier velocity, Geophysical Research Letters, 41, 7209–7216, https://doi.org/https://doi.org/10.1002/2014GL061836, 2014.

Moon, T. A., Gardner, A. S., Csatho, B., Parmuzin, I., and Fahnestock, M. A.: Rapid Reconfiguration of the Greenland Ice Sheet Coastal Margin, Journal of Geophysical Research: Earth Surface, 125, e2020JF005 585, https://doi.org/https://doi.org/10.1029/2020JF005585, 2020.

https://doi.org/10.5194/essd-2026-221
Preprint. Discussion started: 13 May 2026

Mouginot, J., Bjørk, A. A., Millan, R., Scheuchl, B., and Rignot, E.: Insights on the Surge Behavior of Storstrømmen and L. Bistrup Bræ, Northeast Greenland, Over the Last Century, Geophysical Research Letters, 45, 11,197–11,205, https://doi.org/https://doi.org/10.1029/2018GL079052, 2018.

Nagler, T., Rott, H., Hetzenecker, M., Wuite, J., and Potin, P.: The Sentinel-1 mission: New opportunities for ice sheet observations, Remote Sensing, https://doi.org/10.3390/rs70709371, 2015.

Rathmann, N. M., Hvidberg, C. S., Solgaard, A. M., Grinsted, A., Gudmundsson, G. H., Langen, P. L., Nielsen, K. P., and Kusk, A.: Highly temporally resolved response to seasonal surface melt of the Zachariae and 79N outlet glaciers in northeast Greenland, Geophysical Research Letters, 44, 9805–9814, https://doi.org/https://doi.org/10.1002/2017GL074368, https://agupubs.onlinelibrary.wiley.com/doi/abs/10.1002/2017GL074368, 2017.

Rignot, E. and Kanagaratnam, P.: Changes in the Velocity Structure of the Greenland Ice Sheet, Science, 311, 986–990, https://doi.org/10.1126/science.1121381, 2006.

Sole, A. J., Mair, D. W. F., Nienow, P. W., Bartholomew, I. D., King, M. A., Burke, M. J., and Joughin, I.: Seasonal speedup of a Greenland marine-terminating outlet glacier forced by surface melt–induced changes in subglacial hydrology, Journal of Geophysical Research: Earth Surface, 116, https://doi.org/https://doi.org/10.1029/2010JF001948, 2011.

Solgaard, A., Kusk, A., Merryman Boncori, J. P., Dall, J., Mankoff, K. D., Ahlstrøm, A. P., Andersen, S. B., Citterio, M., Karlsson, N. B., Kjeldsen, K. K., Korsgaard, N. J., Larsen, S. H., and Fausto, R. S.: Greenland ice velocity maps from the PROMICE project, Earth System Science Data, 13, 3491–3512, https://doi.org/10.5194/essd-13-3491-2021, https://essd.copernicus.org/articles/13/3491/2021/, 2021.

Solgaard, A. M. and Kusk, A.: Greenland Ice Velocity from Sentinel-1 Edition 5, https://doi.org/10.22008/FK2/K70OPK, https://doi.org/10.22008/FK2/K70OPK, 2026.

Solgaard, A. M., Rapp, D., Noël, B. P. Y., and Hvidberg, C. S.: Seasonal Patterns of Greenland Ice Velocity From Sentinel-1 SAR Data Linked to Runoff, Geophysical Research Letters, 49, e2022GL100 343, https://doi.org/https://doi.org/10.1029/2022GL100343, https://agupubs.onlinelibrary.wiley.com/doi/abs/10.1029/2022GL100343, e2022GL100343 2022GL100343, 2022.

Sugiyama, S., Tsutaki, S., Sakakibara, D., Asaji, I., Kondo, K., Wang, Y., Podolskiy, E., Jouvet, G., and Funk, M.: GPS, AWS and glacier front position data from Bowdoin Glacier, https://doi.org/10.17632/nd39zk6fhh.1, 2024.

Sugiyama, S., Tsutaki, S., Sakakibara, D., Asaji, I., Kondo, K., Wang, Y., Podolskiy, E., Jouvet, G., and Funk, M.: Ice speed of a Greenlandic tidewater glacier modulated by tide, melt, and rain, The Cryosphere, 19, 525–540, https://doi.org/10.5194/tc-19-525-2025, https://tc.copernicus.org/articles/19/525/2025/, 2025.

Thomas, R. H., Csathó, B. M., Gogineni, S., Jezek, K. C., and Kuivinen, K.: Thickening of the western part of the Greenland ice sheet, Journal of Glaciology, 44, 653–658, https://doi.org/10.3189/S002214300000215X, 1998.

Vandecrux, B., MacFerrin, M., Machguth, H., Colgan, W. T., van As, D., Heilig, A., Stevens, C. M., Charalampidis, C., Fausto, R. S., Morris, E. M., Mosley-Thompson, E., Koenig, L., Montgomery, L. N., Miège, C., Simonsen, S. B., Ingeman-Nielsen, T., and Box, J. E.: Firn data compilation reveals widespread decrease of firn air content in western Greenland, The Cryosphere, 13, 845–859, https://doi.org/10.5194/tc-13-845-2019, 2019.

Vijay, S., Khan, S. A., Kusk, A., Solgaard, A. M., Moon, T., and Bjørk, A. A.: Resolving Seasonal Ice Velocity of 45 Greenlandic Glaciers With Very High Temporal Details, Geophysical Research Letters, 46, 1485–1495, https://doi.org/https://doi.org/10.1029/2018GL081503, 2019.

https://doi.org/10.5194/essd-2026-221
Preprint. Discussion started: 13 May 2026

Wehrlé, A., Lüthi, M. P., Kneib-Walter, A., Nap, A., Rousseau, H., Jouvet, G., and Walter, F.: Velocity and Calving Response of a Major Greenland Ice Stream To a Lake Drainage Event, Nature Geoscience, https://doi.org/10.1038/s41561-025-01858-2, http://dx.doi.org/10.1038/s41561-025-01858-2, 2025.

Westerweel, J. and Scarano, F.: Universal outlier detection for PIV data, Experiments in Fluids, 39, 1096–1100, https://doi.org/10.1007/s00348-005-0016-6, 2005.

Wuite, J., Nagler, T., Hetzenecker, M., and Rott, H.: Ten years of polar ice velocity mapping using Copernicus Sentinel-1, Remote Sensing of Environment, 332, 115 092, https://doi.org/https://doi.org/10.1016/j.rse.2025.115092, https://www.sciencedirect.com/science/article/pii/S0034425725004961, 2026.